GEOPHYSICS®

The Effect Of Pressure On Acoustic (1-20 Khz) Velocity And Attenuation During The Melting Of Ice-Bearing Sand

Journal:	*Geophysics*
Manuscript ID:	GEO-2025-0466
Manuscript Type:	Advances in Rock Physics
Keywords:	acoustic, attenuation, compressional wave (P-wave), rock physics, velocity analysis
Manuscript Focus Area:	Rock Physics

DOUBLE-ANONYMOUS REVIEW

THE EFFECT OF PRESSURE ON ACOUSTIC (1-20 KHZ) VELOCITY AND ATTENUATION DURING THE MELTING OF ICE-BEARING SAND

Hanif S. Sutiyoso[1,2,*], Sourav K. Sahoo[2], Ismael H. Falcon-Suarez[2], Laurence J. North[2], Timothy A. Minshull[1], Angus I. Best[2]

[1]School of Ocean and Earth Science, University of Southampton, Southampton, UK.

[2]National Oceanography Centre Southampton, Southampton, UK.

[*]*Corresponding author: Hanif S. Sutiyoso, hanifsans@noc.ac.uk, https://orcid.org/0000-0002-3111-2414*

Original paper date of submission: June 2025

ABSTRACT

Acoustic velocity and attenuation in ice-bearing sediments are strongly influenced by ice and water saturations and can vary with frequency, but the mechanisms linking acoustic response to ice content and morphology remain poorly understood. We measured velocity and attenuation in ice-bearing sand using an acoustic pulse tube, which allowed multifrequency analysis, under effective pressures of 2.5, 5.0, and 7.5 megapascals. Our experiments simulated thawing permafrost conditions at depths of up to 450 meters. As the ice melted, acoustic velocity decreased and attenuation increased, with the most pronounced changes observed at lower pressures. These changes also varied with frequency, especially at higher frequencies. Comparisons with three-phase Biot models suggest that velocity is mainly affected by ice saturation, while attenuation is also influenced by ice morphology (i.e., whether it is pore-filling or cementing) and by the permeability of the sediment frame. These results demonstrate that low-frequency acoustic measurements under controlled conditions can provide insights into the effects of ice saturation, distribution, and morphology on acoustic behavior in ice-bearing sediments that are relevant to field experiments. Our work supports more effective use of acoustic data for permafrost monitoring and highlights the importance of considering both ice saturation and microstructural characteristics when assessing the acoustic properties of ice-bearing sediment.

INTRODUCTION

The elastic properties of ice-bearing sand are of great interest in both geotechnical engineering and environmental science, particularly in permafrost settings (e.g., Bustamante et al., 2023; Kang et al., 2021; Oswell, 2011). Permafrost, or permanently frozen ground, is a critical component of the cryosphere, impacting infrastructure stability (e.g., Hjort et al., 2018) and global climate dynamics (e.g., Schuur et al., 2015). In a warming climate, methane emissions from permafrost degradation are expected to rise (Meredith et al., 2022). In order to monitor and address

these environmental challenges, it is important to be able to link elastic wave properties to ice content (Hilbich et al., 2022).

Elastic wave velocity and attenuation vary with frequency, and this variation affects the interpretation of seismic survey and sonic log data, as well as data generated by laboratory experiments. Elastic properties are also sensitive to pore fluid composition and content (e.g., Emerson and Foray, 2006; Rubino and Holliger, 2012; Sutiyoso et al., 2024) and to the state of stress as represented by confining and pore pressures (Alkire and Andersland, 1973; Falcon-Suarez et al., 2019). Understanding these dependences is therefore essential for comparison of elastic property data from different types of experiment (Kolsky, 1964). Most laboratory studies are conducted at ultrasonic frequencies (150 kHz to 1 MHz; e.g., Dou et al., 2016; Li and Matsushima, 2024; Matsushima et al., 2016) that differ greatly from those of field measurements. To fill this gap, further research is needed at frequencies closer to those of field measurements, such as sonic frequencies used in borehole logging.

Laboratory data serve to validate and enhance rock physics models that predict how ice saturation, distribution, and morphology in porous media influence the mechanical and acoustic properties of ice-bearing sediments (e.g., Li and Matsushima, 2024; Matsushima et al., 2016). A terminology first introduced by Dvorkin et al. (1999) for high-porosity ocean-bottom sediments and later adapted for gas hydrates by Helgerud et al. (1999), ice morphologies are categorized into non-cementing and cementing types based on their interaction with the sediment matrix. In non-cementing morphology, ice does not bond to the sediment framework. Within this category, pore-floating ice grows freely in pore spaces without connecting grains, while pore-bridging ice physically spans the spaces between adjacent grains and may contribute to frame support (Hu et al., 2014; Priest et al., 2009). In contrast, cementing morphology involves ice that bonds directly to sediment grains, either at grain contacts (contact cementing) or as a coating around grains (grain coating) (Best et al., 2013; Ecker et al., 1998; Helgerud et al., 1999). Cementing morphologies enhance load-bearing capacity, significantly influencing the elastic properties of sediment. The

concept of morphology is applied in several existing rock physics models, including those based on Biot's (1956a, 1956b) theory. Such models may consider two phases (sediment and pore fluid) or three phases (sediment, ice or hydrate, and pore fluid; e.g., Leclaire et al., 1994; Marín-Moreno et al., 2017). Because ice-bearing and hydrate-bearing sediments share similar physical properties, models developed for one system are often applicable to the other (Helgerud et al., 1999), providing a framework for predicting elastic wave behavior in frozen and partially frozen media.

Permafrost can extend up to 365 m below the surface (Dobiński, 2020) with estimated confining pressures ranging from 4.9 to 6.2 MPa (Kawasaki et al., 1983). Hence, effective monitoring and interpretation of permafrost environments requires an understanding of the combined effect of ice saturation, distribution, and morphology and of pressure changes on seismic wave propagation at a given frequency. Here, we investigate the acoustic wave properties of ice-bearing sands at different pressures within the sonic frequency range (1-20 kHz). The acoustic pulse tube setup and methodology described by Sutiyoso et al. (2025) were applied to extend a dataset at 2.5 MPa effective pressure to two additional effective pressures of 5.0 and 7.5 MPa. We assess our experimental results using three-phase rock physics models to provide new insights into ice content estimates from seismic or sonic log data at in situ pressures of typical permafrost formations.

MATERIALS AND METHODS

Ice-bearing sand sample

We used clay-free Leighton Buzzard sand with a mean grain diameter of 100 μm, chosen for its similarity to the grain size of typical permafrost sands (e.g., Fuchs et al., 2018; Liu et al., 2023; Strauss et al., 2012). The sand was packed in a 0.5 m long PVC pipe and sealed with PVC endcaps to enable uniform confining pressure. The acoustic impedance of the PVC material is 2.9 x 10^6 kg m^{-2} s^{-1} (Selfridge, 1985), while the impedance of the sand pack ranges from 2.2 to 6.8 x

10^6 kg m^{-2} s^{-1}, depending on whether it is water-saturated or ice-bearing (Kang et al., 2021; Schumann et al., 2014; Sutiyoso et al., 2025).

To prepare the sample, we poured sand into the PVC pipe, compacting it in layers for even compaction and scratching the surface between layers to minimize impedance contrasts. The porosity of the sand pack was 41 ± 0.1%, calculated from the wet-dry mass balance, with uncertainties determined through error propagation. Once compacted, we gradually added a pre-calculated amount of de-ionized water and tapped the pipe to release air bubbles. This process helped in reducing gas bubbles in the ice, resulting in more consistent laboratory measurements (McCutchan and Johnson, 2022). After fully saturating the sample, we sealed it and let the water distribute for 24 hours. Although the sample was saturated, this step helped to balance pore pressure and promote more uniform water distribution across the packed layers through slow internal movement driven by gravity and capillary forces (Snehota et al., 2015). Then, we froze the sample at -10°C for 48 hours. Further details about the sample preparation can be found in Appendix A.

Ice saturation (S_i) was inferred from the elapsed melting time during measurements. We established a baseline by measuring velocity and attenuation in the fully melted state ($S_i = 0$). The initial ice saturation was assumed to be $S_i = 1$, although some unfrozen water likely remained in thin films around the grains (Watanabe and Mizoguchi, 2002). Due to the time needed to reach the target pressure inside the pulse tube after transfer of the sample from the chest freezer, measurements at full ice saturation were not possible, so a regression model was used to estimate velocity and attenuation at $S_i = 1$. Ice saturation was calculated using an empirical relationship, $S_i = 1 - \left(\frac{t}{T}\right)^n$, where t is the time elapsed during measurement (in seconds), T is the total time for complete melting (determined by the velocity and attenuation at the fully melted state), and n is an empirical parameter describing the exponential relationship between ice melting and time. The parameter n was derived by comparing experimental results with rock physics models and

minimizing an objective function. Additional details on the ice saturation estimation are provided in Appendix B.

Note that the volumetric expansion of ice might have introduced errors in saturation estimation (French, 2007), along with the potential unfrozen water in the form of thin films (Dash et al., 1995; Watanabe and Mizoguchi, 2002). To account for these uncertainties, we have included error bars in our figures, based on a conservative 9% error estimate that considers these sources of error (French, 2007).

Pulse tube measurements

We measured velocity and attenuation (inverse quality factor, $1/Q$) using a 4.5-meter-long acoustic pulse tube with variable-frequency chirp signals within the range of 1-20 kHz. The tube uses a piezoelectric transducer located at the base of a stainless-steel cylinder filled with water to propagate plane waves along the tube's axis, based on an acoustic waveguide concept (Redwood, 1960). The sand-ice sample was suspended in the water-filled tube about halfway down. We collected new acoustic measurements at effective pressures (P_{eff}) of 5.0 and 7.5 MPa under a controlled temperature of 19°C, and included previously reported data at 2.5 MPa (from Sutiyoso et al., 2025). Assuming a permafrost density of 1700 kg m^{-3} (Kawasaki et al., 1983), our experiments simulated conditions similar to those of thawing permafrost at depths of approximately 150 – 450 m. While permafrost has been reported to extend to depths of up to 365 m (Dobiński, 2020), a higher-pressure limit was selected to account for variability in permafrost density and to provide a conservative upper bound. Our temperature setting reflects an extreme surface warming scenario (Kim et al., 2024).

At each effective pressure, we allowed the sample to thaw during the measurement process, enabling us to track changes in acoustic wave properties as the ice gradually melted. After completing the measurements at one pressure, the sample was removed from the pulse tube and rested for 24 hours at atmospheric pressure to reduce residual effects from compression under

confining pressure, then re-frozen inside a chest freezer to restore the initial frozen condition before moving to the next pressure step. Although this method freezes the sample before applying pressure, unlike natural permafrost, which freezes gradually under stress, it provides controlled conditions to isolate pressure effects on acoustic properties. Our measurements covered the full melting process, from frozen to completely thawed states. This experimental approach ensures the results remain applicable to a wide range of natural permafrost conditions, including regions with thick permafrost or elevated overburden stress.

For each measurement, we recorded signal amplitude as voltage across the ice saturation stages. We applied a Fast Fourier Transform to deconvolve the raw signals and obtain the impulse response, followed by time-domain gating to eliminate extraneous reflections. Then, we applied a non-linear inversion model incorporating the scattering matrix method to determine the complex velocity, and attenuation was derived according to Equation 1 (Mavko et al., 2009). The inversion incorporated reference (sample-less) pulse tube measurements to eliminate transducer transfer functions and temperature dependency.

$$Q^{-1} = \frac{1 - e^{-2\pi\frac{v_1}{v_2}}}{2\pi} \quad (1)$$

where V_1 and V_2 are the real and imaginary velocities, respectively.

The pulse tube was calibrated by comparing experimental measurements with theoretical transmission coefficients to determine velocity and attenuation errors, following the method of McCann et al. (2014). The relative experimental uncertainties were ± 2.4% for velocity and ± 5.8% for attenuation. Calibration measurements using a nylon rod also agreed with ultrasonic data extrapolated to the sonic range using a standard linear solid model (Kolsky, 1964), with less than ±1% difference. Figure 1 compares the compressional velocity measured in this study with published values for similar sand packs. Our velocities are comparable with lower-frequency measurements (e.g., Kang et al. (2021) at seismic frequencies), and are lower than those measured at ultrasonic frequencies (Dou et al., 2016; Spangenberg et al., 2018; Yang et al., 2021). Nakano

and Arnold (1973) reported measurements on saturated Ottawa sand with a grain size of 1 mm (about ten times larger than in our samples), which explains their slightly lower velocity. Overall, these comparisons demonstrate that our results are within a reasonable range of published data, given differences in measurement frequency and experimental design. Figure 2 presents the schematic diagrams of the pulse tube and examples of measured and deconvolved signals. Further details of the experimental setup and data processing are given by North and Best (2015) and Sutiyoso (2025).

To ensure accurate measurements, we determined cut-off frequencies based on the requirement that at least half of the wavelength should propagate through the 0.5-meter-long sample, with wavelengths calculated as velocity divided by frequency. The corresponding cut-off frequencies are 4.0 kHz for P_{eff} = 2.5 MPa and 4.8 kHz for the 5 and 7.5 MPa data, respectively, resulting in half-wavelengths of 0.41 - 0.50 m. Below these frequencies, the half-wavelengths exceed the sample length, and thus may not fully represent the bulk sample conditions. Aside from frequency dependence analysis, we mainly focus on the experimental results at 10 kHz, the mid-bandwidth frequency. Nevertheless, data below the cut-off are still shown because they provide useful context for frequency-dependent trends and help identify the onset of reliable wave propagation within the measurement band.

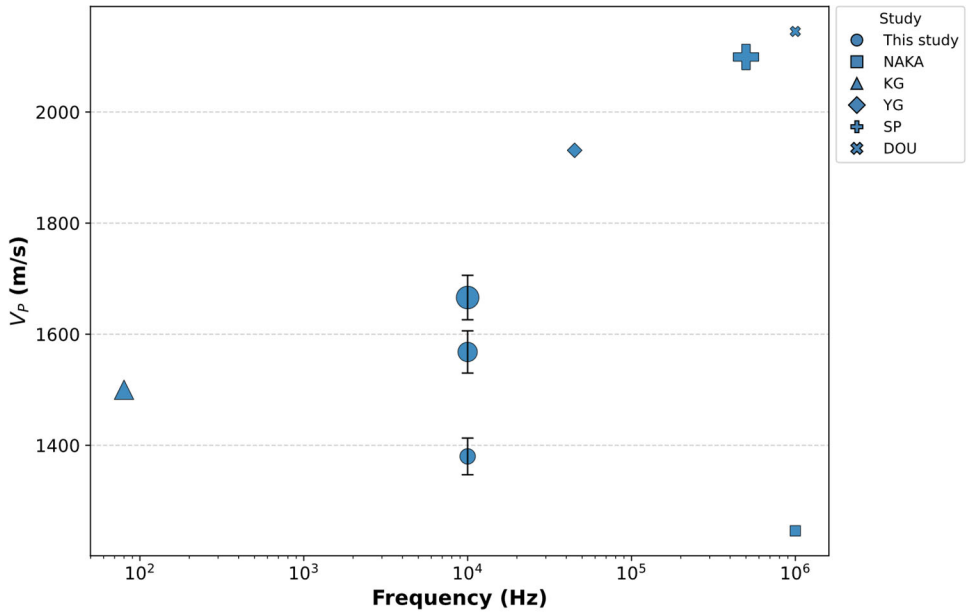

Figure 1 *Comparison of compressional velocity (V_P) of water-saturated sand measured in this study with values reported in published studies. The three data points for this study represent measurements at different effective pressures (2.5, 5.0, and 7.5 MPa), with error bars indicating experimental uncertainty. Marker size represents the confining pressure, ranging from atmospheric pressure to 10 MPa. The study codes are as follows: KG (Kang et al., 2021), YG (Yang et al., 2021), SP (Spangenberg et al., 2018), DOU (Dou et al., 2016), and NAKA (Nakano and Arnold, 1973).*

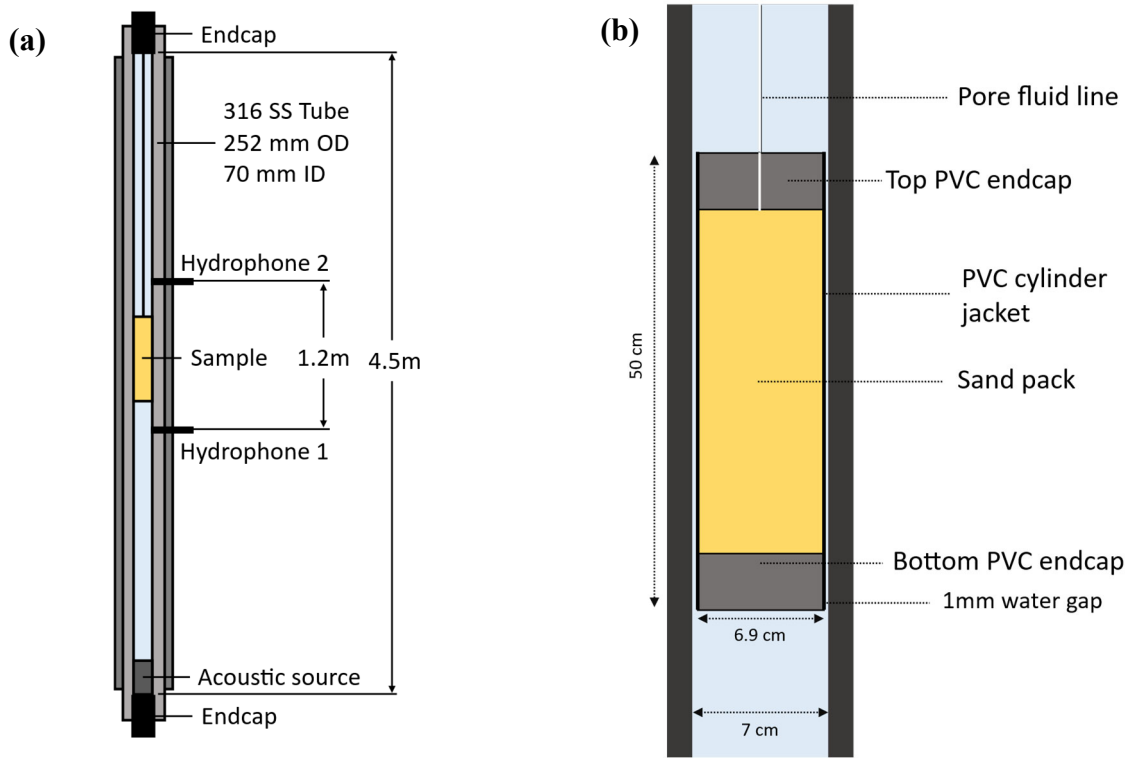

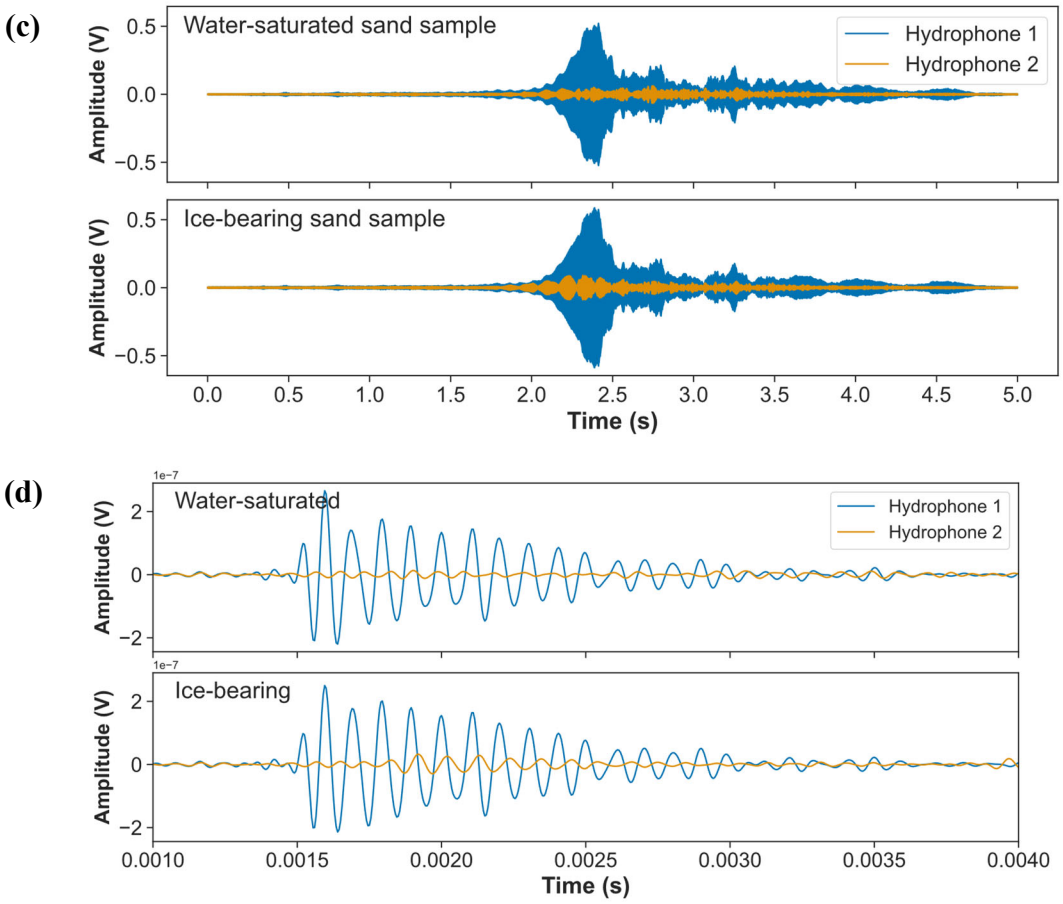

Figure 2 *Experimental apparatus and resulting raw and processed data: (a) Schematic diagram of the pulse tube with dimensions; (b) details of the PVC-jacketed sample inside the water-filled pulse tube; (c) raw time-series signals acquired during measurements; (d) deconvolved signals for water-saturated and ice-bearing sand samples on both hydrophones (see panel (a) for hydrophone positions).*

Rock physics models

We used two rock physics models incorporating Biot's theory to investigate the mechanisms underlying the melting process in ice-bearing sand. The first, developed by Leclaire et al. (1994), extends Biot's (1956a, 1956b) theory to predict elastic wave behavior in frozen media comprising sediment matrix, ice, and unfrozen water. This model assumes that a thin film of water around the grains prevents direct contact between the sediment and ice, except in fully frozen conditions. The second model involves substituting hydrate with ice in the hydrate-bearing effective sediment (HBES) model (Marín-Moreno et al., 2017), which then treats pore-filling ice

as part of the pore fluid and cementing ice as part of the sediment frame. In both models, the elastic moduli of the sediment frame vary with effective pressure. In the HBES model, this variation follows the Hertz-Mindlin contact theory (Mindlin, 1949). In Leclaire et al.'s (1994) model, it follows Biot's theory. Thus, the models explicitly account for the influence of effective pressure on both velocity and attenuation.

We extended the HBES model by incorporating additional effective medium approximations by Brie et al. (1995) and Voigt (1889), alongside the existing Reuss (1929) approximation, to calculate pore fluid bulk moduli and assess how ice distribution (whether uniform or patchy) affects acoustic properties. We also investigated the effect of ice morphology on acoustic velocity and attenuation, defined by the proportion of pore-filling (PF) and cementing ice (C = 1 – PF). The HBES model treats cementing ice as part of the sediment frame, using the Voigt-Reuss-Hill average for bulk and shear moduli, as described by Ecker et al. (2000). In contrast to the classic approach of Dvorkin et al. (1999) and Helgerud et al. (1999), in which cementing ice replaces sand grains in the matrix, the HBES model preserves this matrix and incorporates a distinction between cementing ice coating or bonding at grain contacts. Unlike gas hydrate, ice lacks microporosity, which is pores smaller than a micron that drives squirt-flow. Therefore, it contributes less to stress-induced attenuation (Best et al., 2013). Thus, we consider the pore-filling and cementing morphologies sufficient to capture the underlying mechanisms controlling acoustic parameters in ice-bearing sediments. The model inputs are provided in Table 1.

Table 1 *Fixed input parameters that are used in all model runs and case-dependent parameters that are used only in HBES model runs.*

Parameter	Value	Units	Reference
Fixed input parameters			
Experimental conditions			
Effective pressure (P_{eff})	2.5, 5.0, 7.5	MPa	
Temperature	19	°C	

Sand sediment properties			
Porosity without ice	0.41		Measured
Critical porosity	0.38		Best et al. (2013)
Sand grain bulk modulus	36×10^9	Pa	Simmons (1965)
Sand grain shear modulus	45×10^9	Pa	Simmons (1965)
Sand grain density	2650	$Kg\ m^{-3}$	Simmons (1965)
Sand grain diameter	10^{-4}	m	Best et al. (2013)
Coordination number	9		Murphy (1982)
Tortuosity	3		Berryman (1981)
Ice grain properties			
Ice bulk modulus	5.5×10^9	Pa	Chang et al. (2021)
Ice shear modulus	2.7×10^9	Pa	Chang et al. (2021)
Case-dependent input parameters			
Pore-filling saturation	0.6 – 1.0		
Sand column permeability	0.3 – 1.1	Darcy	

RESULTS

Experimental results

Figure 3 shows the evolution of the elastic wave attributes (velocity, V_P and attenuation, $1/Q_P$), for the whole ice saturation (S_i) range at a frequency of 10 kHz and is representative of the behavior at other frequencies measured. Velocity decreases as ice saturation decreases across all effective pressure (P_{eff}) conditions (Figure 3a). The slope of the curve is steeper in the ice saturation range $S_i > 0.5$, and the change of V_P with S_i within this S_i range is 20% larger at 2.5 MPa than at 7.5 MPa. At high ice saturation ($S_i > 0.9$), velocities at P_{eff} of 2.5 and 5 MPa are comparable and slightly higher than at 7.5 MPa by ~300 m/s. At zero saturation ($S_i = 0$), velocity is highest at 7.5 MPa, followed by 5 MPa and 2.5 MPa, as expected for water-saturated sand packs (Zimmer et al., 2002). The overall velocity drop from high to zero saturation is largest at 2.5 MPa (~3000 m/s) and smaller at 5 MPa and 7.5 MPa (~2500 m/s), suggesting that ice content exerts a stronger influence on the elastic properties at lower pressure.

Attenuation increases as ice melts from maximum saturation to $S_i \sim 0.2$ at 2.5 MPa, and to $S_i \sim 0.7$ at 5 and 7.5 MPa, after which it remains relatively constant down to $S_i = 0$ across all pressures (Figure 3b). The saturation corresponding to attenuation peak increases by ~0.5 with increasing effective pressure. This observation suggests that at higher effective pressure, the sand grains are more compact due to closer grain contact, making the sand matrix more resistant to deformation as the ice melts (Zimmer, 2003).

Across ice saturation levels, the 2.5 MPa data consistently show the highest attenuation, followed by the 5 and 7.5 MPa data. At $S_i > 0.7$, attenuation values are similar across all pressures, within the range of data variability. However, as the ice melts, attenuation becomes more sensitive to pressure, with a maximum variation of ~0.015 at $S_i \sim 0.3$. The slope of the attenuation curve steepens more as ice melts at $P_{eff} = 2.5$ MPa and less for the 5 and 7.5 MPa cases, similar to the behavior of the velocity curves.

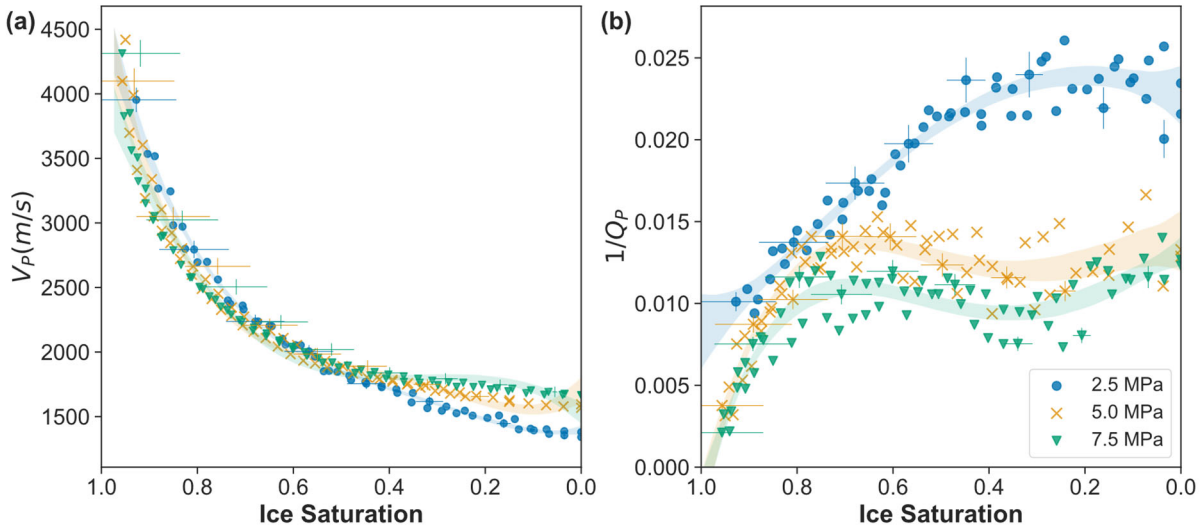

Figure 3 *Variations in P-wave velocity (V_P) and attenuation ($1/Q_P$) at 10 kHz during the ice melting process at various effective pressures, with shaded areas representing fourth-order polynomial regression models with a confidence interval of 90% (R^2 of 0.99, 0.98, 0.98 for velocity and 0.94, 0.82, 0.79 for attenuation at 2.5, 5, and 7.5 MPa, respectively). Error bars are plotted every 10 data points.*

Velocity varies slightly with frequency, showing similar maxima at ~18 kHz and S_i = 0.9 for all three pressures (Figure 4a). These maxima could be related to ice redistribution during early melting that results in changes at cm-scale, given the wavelength of 0.1 m at that frequency. At high ice saturations (mainly S_i > 0.9), velocity generally decreases with increasing frequency, whereas at intermediate saturations (S_i ~ 0.6-0.9), velocity tends to increase with frequency, with some dependence on pressure (Figure 5). These contrasting trends indicate that the dominant controls on frequency-dependent velocity evolve as the pore structure transitions from ice-dominated to increasingly water-connected during thawing. This transition may reflect the squirt-flow type behavior as thawing produces partially connected fluid pathways, altering the pore-scale pressure equilibration at higher frequencies (Müller et al., 2010).

Attenuation shows the same trend with frequency as with velocity at low P_{eff} (2.5 MPa), except at S_i = 0. When P_{eff} increases, attenuation shows complex patterns for the whole frequency range (Figure 4b). This frequency sensitivity may relate to the squirt flow processes as suggested

above, because partially connected water pockets could also increase energy loss at specific frequencies (Carcione et al., 2003). However, the variability observed in the trends for different pressures suggests that stress-induced mechanical phenomena at the grain scale also affect pore connectivity. At S_i = 0, attenuation varies similarly above 5 kHz across all pressures, with peaks around 13 - 14 kHz. These variations at higher frequencies may be influenced by small-scale heterogeneities, also seen in the velocity data.

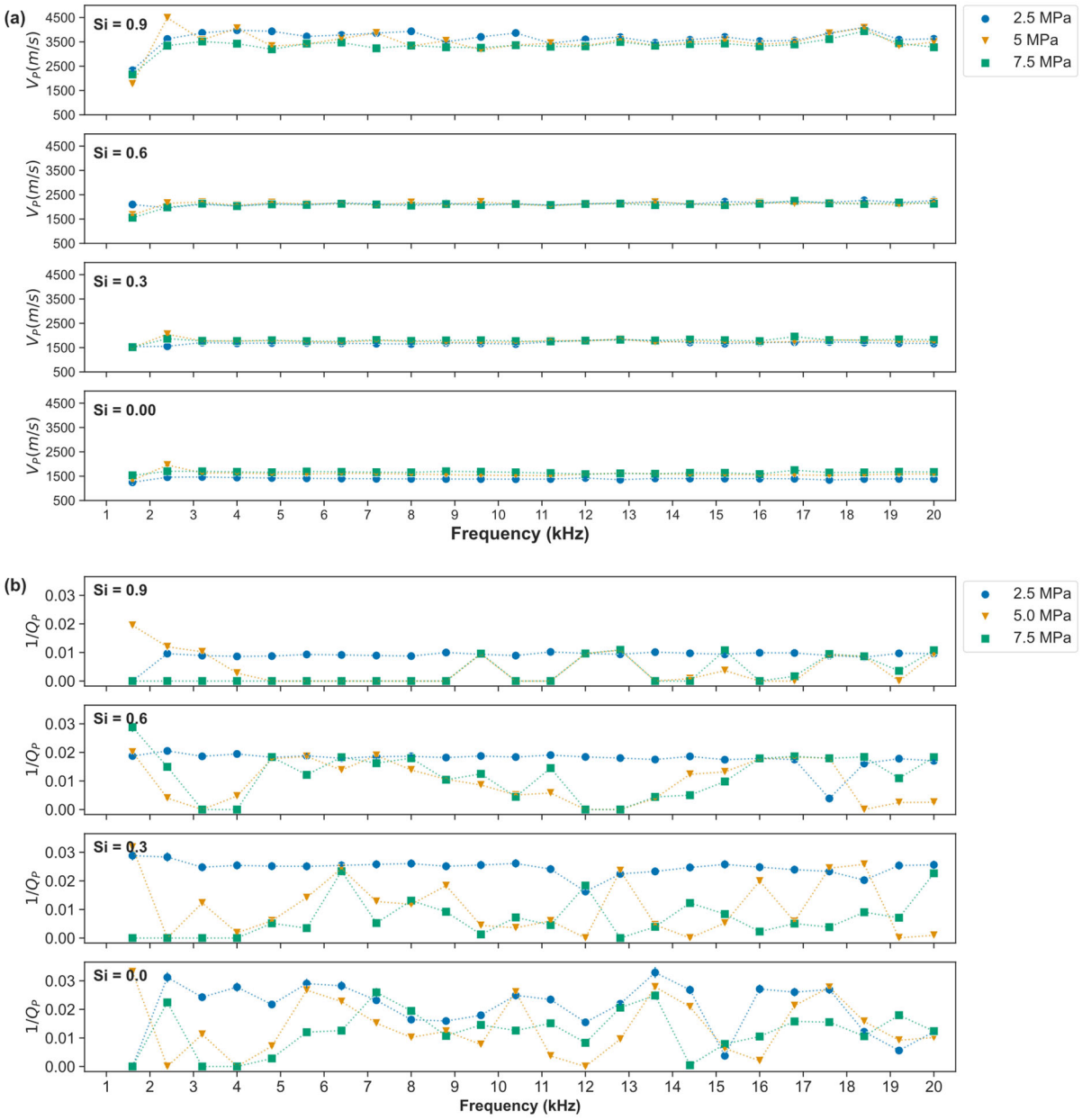

Figure 4 *Experimental results: a) P-wave velocity (V_P) and b) attenuation ($1/Q_P$) spectra at selected ice saturations (S_i). The error bars are smaller than the symbol sizes. Legends represent effective pressures in megapascals (MPa).*

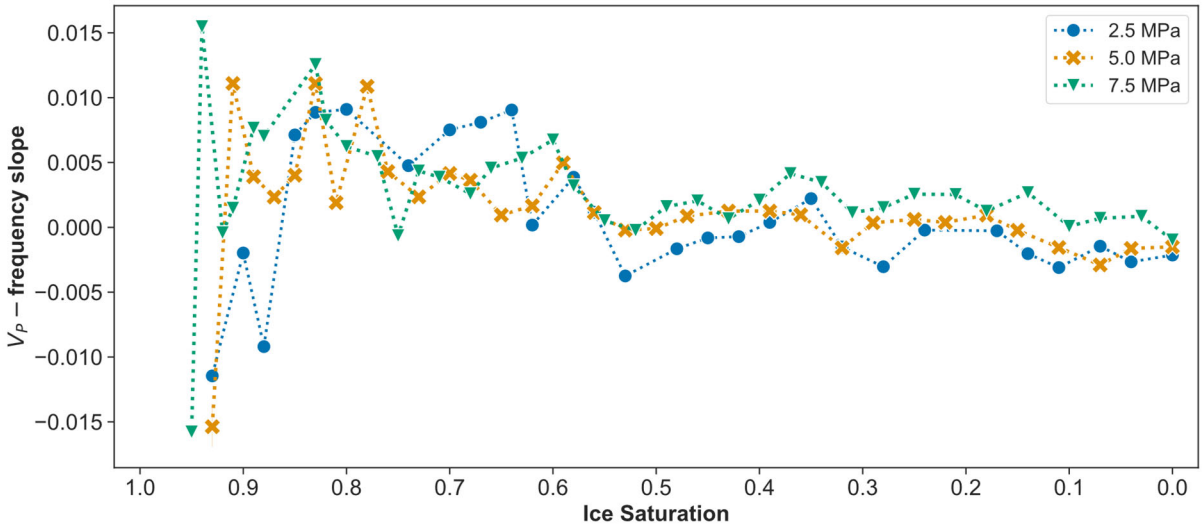

Figure 5 *Regression slope of P-wave velocity (V_P) versus frequency between the cut-off and maximum (20 kHz) frequencies as a function of ice saturations and effective pressures. Positive slopes indicate velocity increasing with frequency, while negative slopes indicate velocity decreasing with frequency. Legends represent effective pressures in megapascals (MPa).*

We also evaluated the relationship between the acoustic parameters and ice saturation at each frequency using Spearman's rank correlation (Figure 6). Specifically, we calculated the correlation coefficients between measured velocity or attenuation values and corresponding ice saturation levels across all saturations at each frequency. This analysis evaluates the sensitivity of each frequency's acoustic response to changes in ice saturation, leveraging the multi-frequency capability of the acoustic pulse tube. Velocity correlates strongly with changes in ice saturation ($r > 0.81$), consistently exceeding the 99% confidence level across all frequencies and effective pressures. As ice saturation decreases, velocity also decreases, as confirmed by the positive correlation.

In contrast, attenuation shows more complex behavior than velocity, and its relationship with ice saturation is not strictly monotonic (Figure 3b). For this reason, the correlation analysis is not intended to quantify a physical trend with saturation but rather to identify the frequency bands

where attenuation responds most consistently to changes in ice content. At 2.5 MPa, attenuation has larger correlation magnitudes and lower measurement uncertainty, producing stronger correlations than at 5 and 7.5 MPa, where values are closer to the detection limit and uncertainties increase. The most robust correlations occur between 5 and 10 kHz, particularly near 7 kHz, indicating that this band provides the clearest and most stable attenuation signal across pressures. These results may highlight the 5-10 kHz band as the most effective range for monitoring attenuation changes in the thawing of ice-bearing unconsolidated sediments, but they also point to limitations at higher pressures where attenuation becomes very small.

At higher pressures and lower ice saturations (5.0 and 7.5 MPa), attenuation values occasionally approached the system's detection limit (<0.01 or $Q > 100$), potentially masking subtle changes in wave-induced fluid flow or permeability. The lower limit for detectable attenuation within our sample arises from the departure from the plane-wave propagation assumed in the data-inversion algorithm. This behavior can also contribute to apparent deviations from the Kramers–Kronig causality principle, which may be amplified by the finite frequency bandwidth of laboratory measurements (Mobley et al., 2000). Despite these limitations, the overall trends remain physically consistent with Biot-type behavior and are relevant for geophysical monitoring, particularly in lower-pressure or higher-saturation settings where Biot flow is more active, as attenuation magnitudes above 0.01 are of practical importance (e.g., Allmark et al., 2018; Parolai et al., 2022).

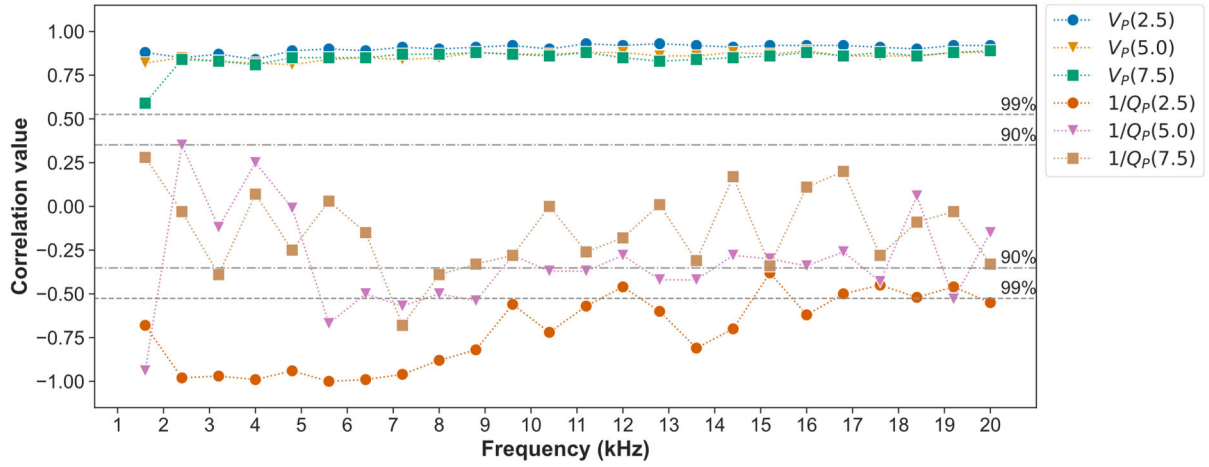

Figure 6 *Spearman's rank correlation coefficients between acoustic properties (P-wave velocity, V_P and attenuation, $1/Q_P$) and ice saturation, calculated at each frequency and effective pressure (in megapascals). The vertical axis ranges from -1 to +1 to accommodate both positive (typically for velocity) and negative (typically for attenuation) correlations. The 90% and 99% confidence level lines apply to both acoustic properties and indicate statistically significant correlations.*

Insight from modeling

Initially, we compared our data to the LeClaire model and to HBES models with entirely pore-filling ice and a permeability of 0.5 D (Fig. 7a). All models predict that velocity decreases with varying rates when ice melts. The Leclaire model predicts the steepest decrease at high saturations ($S_i > 0.8$), followed by the HBES models with Voigt, Brie, and Reuss approximations. These differences reflect the influence of assumed ice distribution on velocity, since the Leclaire model assumes the most heterogeneous (patchy) distribution, while HBES-Reuss represents the most uniform, with Voigt and Brie in between.

At P_{eff} = 2.5 MPa, the experimental velocities align well with the HBES-Voigt model, particularly at intermediate saturations (S_i = 0.8 to 0.4), but shift towards the Leclaire model at lower saturations ($S_i < 0.2$). At 5 and 7.5 MPa, experimental velocities are still in good agreement with HBES-Voigt at most saturations but are closer to the Leclaire model than at 2.5 MPa.

Higher effective pressure causes experimental velocities to fit closer to the Leclaire prediction at intermediate saturations (e.g., S_i = 0.8 to 0.4), likely due to pressure-induced changes

in pore structure (Zimmer et al., 2002). As grain contact increases under higher pressure, ice in smaller pore spaces may melt at different rates compared to larger spaces, where the availability of pore fluid for heat transfer differs, promoting uneven melting rates (Abbasi et al., 2022; De Lemos, 2012).

All modeled attenuations increase with melting, although the trends are less straightforward than for velocities (Figure 7b). At 5 and 7.5 MPa, attenuation increases from S_i = 1.0 to ~0.4, then levels off or decreases. At 2.5 MPa, similar patterns only occur in the Leclaire and HBES-Voigt models, while the HBES-Brie and Reuss models show near-continuous increases. While ice distribution affects velocity at all pressures, attenuation becomes less sensitive to distribution at higher pressures in the HBES models. We also observed shifts in the modeled attenuation peaks, although these differed from the experimental trends. For example, the HBES-Voigt peak shifts from lower to higher ice saturation as effective pressure increases, moving from S_i = 0.125 at 2.5 MPa to S_i = 0.375 at 7.5 MPa.

At 2.5 MPa, the measured attenuation aligns well with the HBES-Voigt model at $S_i < 0.6$ but exceeds the predictions of this model at higher saturations, possibly indicating an additional loss mechanism beyond Biot theory. At 5 and 7.5 MPa, the experimental trends become more complex. Measured attenuation is higher than predicted at $S_i > 0.6$, and more variable at lower saturations, but still closer to the HBES models than to the Leclaire model.

We then investigated the effects of ice morphology and sediment frame permeability using the HBES-Voigt model, which showed the best fit to experimental data. The following discussion focuses on attenuation, as velocity does not change significantly with either parameter (see Appendix B). Modeled attenuation increases with pore-filling (PF) saturation across all saturations and pressures (Figure 7c). This effect is strongest at 2.5 MPa, especially at low ice saturations ($S_i < 0.4$). Measured attenuation aligns well with the higher PF saturation curves at low ice saturations ($S_i < 0.6$), suggesting a transition from cementing ($C = 1 - PF$) at higher saturation to pore-filling at lower saturations. This trend is less pronounced at higher pressures. These variations offer insight

into how acoustic properties are affected by melting, particularly at lower ice saturations where the formation is potentially less uniform.

Modeled attenuation also varies with permeability at most ice saturations ($S_i < 0.8$) across all pressures (Figure 7d). Higher permeability leads to higher attenuation, especially at low saturation ($S_i < 0.4$), consistent with Biot's global flow theory, where greater relative motion between the solid matrix and viscous fluid leads to higher attenuation. Measured attenuation mostly corresponds to model permeabilities of 0.3 - 0.6 D. These values are reasonable for tightly packed ice-bearing sand in permafrost conditions, where values of around 0.01 – 1.01 D are reported by Sizemore and Mellon, 2008). The increase in permeability may explain the distinct increase in measured attenuation at lower ice saturation ($S_i < 0.3$), especially at 7.5 MPa. As ice melts, liquid water content and permeability increase due to more spaces becoming available (Mahabadi et al., 2019), thus allowing greater pore fluid movement relative to solid grains, which consequently increases attenuation (Lee et al., 2024).

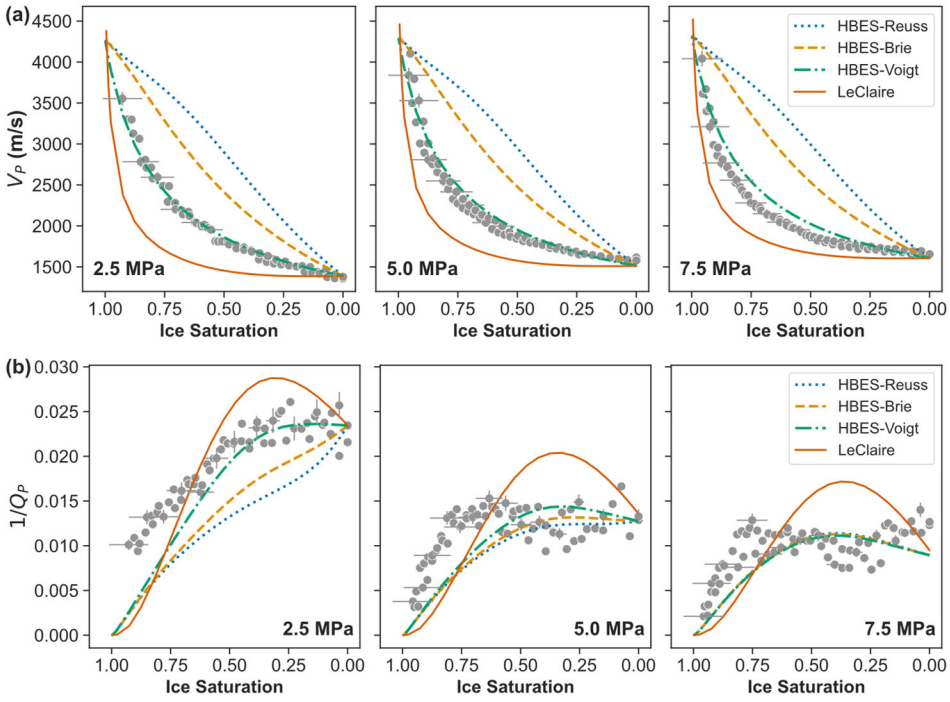

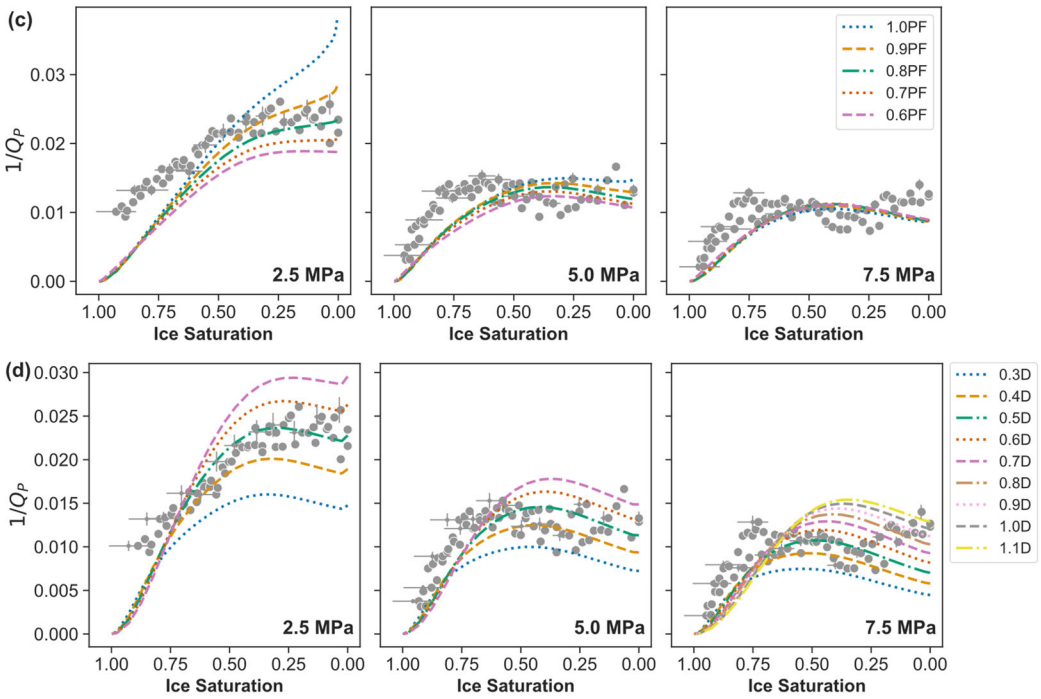

Figure 7 *Comparison of experimental data and model results for P-waves at 10 kHz: a) velocity (V_P) and b) attenuation ($1/Q_P$). In the HBES models, the pore-filling saturation PF is 1.0 and the permeability is 0.5 D; c) attenuation at different PF (with the remainder of S_i as cementing ice, i.e., 1 - PF); and d) attenuation at different permeabilities for PF = 1.0. Results in c) and d) are modeled using the HBES model with Voigt approximation. Cross-error bars are plotted every 15 experimental data points.*

DISCUSSION

Ice content in ice-bearing sand affects both acoustic velocity and attenuation across all tested effective pressures. As ice melts, velocity decreases and attenuation increases, which is consistent with previous studies at ultrasonic (e.g., Matsushima et al., 2016; Yang et al., 2021) and sonic (Sutiyoso et al., 2025) frequencies. We found that ice saturation could mask the stress effect within the measured range, as the V_P-S_i trends are similar across all effective pressures. In contrast, attenuation is more pressure-dependent, especially at high ice saturations. At low pressure, the sand may experience more strengthening from ice formation, thus losing more structural support as the ice melts (i.e., decreasing frame bulk modulus), which affects both velocity and attenuation even down to fully melted conditions ($S_i = 0$). These findings highlight the value of conducting acoustic measurements in ice-bearing sediments at a variety of effective pressures. At lower effective

pressures, grain-to-grain contacts may be forced apart by ice-induced expansion during crystallization (Alkire and Andersland, 1973). This effect is also observed with gas hydrates (e.g., Priest et al., 2021). Because water expands upon freezing, ice formation could dilate the sand pack at lower pressures, with grains settling back into contact as the ice melts. In contrast, higher pressures may restore grain contact before melting, possibly deforming any ice initially formed. As a result, ice melting exhibits the largest acoustic shift at 2.5 MPa. At higher pressures (5.0 and 7.5 MPa), stronger grain contacts diminish the influence of ice in supporting the matrix during the melting process. In other words, acoustic propagation is more influenced by ice-water interactions at lower pressures and by the sand frame-water system at higher pressures.

Velocity data show an inflection point (where velocities under all effective pressures intersect) at $S_i \sim 0.5$ (Figure 3). This observation may suggest that load-bearing ice is significant for $S_i > 0.5$, which would strongly depend on the degree of dilation during the ice-forming stage. Across pressures, attenuation at $S_i > \sim 0.8$ shows similar values, likely because Biot-type flow is minimal due to pore-clogging effects, resulting in small but finite losses. Since ice is assumed to be non-microporous, attenuation is essentially controlled by global Biot fluid flow, with minimal contribution from sub-microporous squirt flow. Consequently, attenuation is largely linked to permeability for a given ice saturation. In addition, attenuation would also reflect ice morphology (e.g., Sahoo and Best, 2021), as ice transitions from a cementing or load-bearing phase to a pore-filling morphology with decreasing saturation. This transition can influence how Biot flow and frame stiffness evolve with pressure and melting. Therefore, attenuation may serve as an indirect diagnostic of both ice saturation and morphology.

Scattering attenuation arising from small-scale heterogeneities, such as patchy ice distribution, may also contribute to the observed acoustic response, particularly at intermediate saturations where impedance contrasts are the highest (Hefner et al., 2006; Wu and Aki, 1985). However, our measurements at sonic frequencies in a homogeneous sand pack suggest that intrinsic attenuation remains dominant. Direct validation of ice structure (e.g., via micro-CT imaging or thin

section analysis) is not feasible due to the sample size and complex configuration of our experimental setup. Nonetheless, the hydrate morphologies represented in HBES have been validated with X-ray computer tomography (Sahoo et al., 2018), and ice is widely recognized as an appropriate analogue for hydrate in this context (Helgerud et al., 2009; Spangenberg et al., 2018), indirectly supporting our assumptions about ice distribution.

The inverse relationship between velocity and attenuation (Figure 8) across all effective pressures is consistent with both model predictions and other experimental observations (e.g., Li and Matsushima, 2024; Yang et al., 2021). This effect results from matrix stiffening at high ice saturations or high effective pressure, which allows acoustic waves to transmit more efficiently, thereby reducing energy loss (Li and Matsushima, 2024; Zimmer et al., 2002). The clear velocity-attenuation trends and good correlations observed for each pressure, even within such a small effective pressure range, suggest that inferring ice saturation at given depths is feasible provided that both P-wave velocity and attenuation can be measured.

Velocity strongly correlates with ice saturation across the entire frequency range (1-20 kHz), while attenuation correlates more strongly at lower frequencies, particularly around 7 kHz (Figure 6). This may be because attenuation at 7 kHz is higher than at adjacent frequencies, making it more detectable by the pulse tube system and leading to a stronger and more reliable correlation at that frequency. Variation at higher frequencies may also be attributed to the heterogeneities of water and ice distribution caused by the thawing process. At these frequencies, attenuation becomes more sensitive to changes in ice content because the shorter wavelengths are comparable in scale to the heterogeneities, making them more apparent. In contrast, at lower frequencies, the longer wavelengths average out these small-scale variations, resulting in a smoother and more predictable relationship between attenuation and ice content (Sutiyoso et al., 2025). In addition, phase-transition effects at ice-water-grain interfaces can further influence acoustic properties (Li and Matsushima, 2024). During thawing at high ice saturations, thin water films forming at grain contacts may soften the sediment matrix, leading to a decrease in acoustic velocity and an increase

in attenuation. While water vapor formation is theoretically possible, the pressure in our experiments (2.5-7.5 MPa) prevents bulk vapor generation (Wagner et al., 2011). Therefore, the observed changes in acoustic response are likely dominated by the general effects of phase transition at ice-water-grain interfaces. These complementary behaviors highlight the potential of velocity and attenuation as dual indicators to estimate ice content in field scenarios, particularly in well-logging applications at similar frequencies (Hearst and Nelson, 1985). Well logs have commonly been used to identify permafrost layers (e.g., Desai and Moore, 1968; Osterkamp and Payne, 1981), and the findings of this study could improve the interpretation of such data by providing a more physically grounded basis for estimating ice saturation.

In summary, velocity strongly correlates with ice saturation across the frequency band, while attenuation exhibits its strongest correlation at lower frequencies, particularly around 7 kHz. These results highlight the importance of selecting an appropriate frequency range to effectively capture frequency-dependent mechanisms related to ice content in ice-bearing sediments. Optimizing measurement frequencies improves our ability to monitor and predict changes in frozen grounds, with broader applications for quantifying and monitoring ice content in permafrost regions (e.g., Hilbich et al., 2022; Lin et al., 2018).

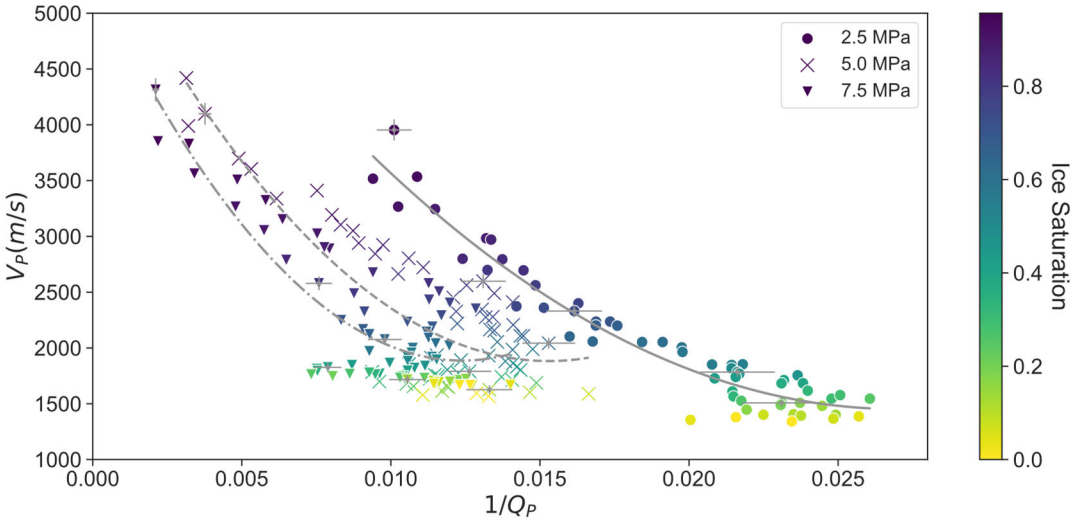

Figure 8 *Variations in P-wave velocity (V_P) and attenuation ($1/Q_P$) at 10 kHz plotted against each other, with lines representing second-order polynomial regression models with R^2 of 0.94, 0.72, and 0.72 at 2.5, 5, and 7.5 MPa, respectively. Marker types represent different effective pressures as shown in the legend. Cross-error bars are plotted every 15 data points.*

While this study tests a range of effective pressures, allowing for insights into multi-depth conditions (approximately 150 – 450 m below the surface, depending on sediment density), we acknowledge that our use of a homogenous sand pack may differ from field conditions, which typically feature variable grain sizes and lithologies. To control sample variability, the same sample was reused across freeze-thaw and re-pressurization cycles. Repeated thermal and mechanical loading may introduce cumulative effects, which we mitigated by allowing the sample to rest between measurements. Subtle impacts may still occur, including sand dilation under pressure, microstructural rearrangements, changes in grain contact bonding due to repeated ice formation, or minor changes in pore geometry. Although direct monitoring of these effects was not possible, their influence is expected to be limited in a homogeneous sand pack, yet they should still be considered when interpreting the results. Additionally, acoustic response may depend on the freezing and melting history (Dou et al., 2016; Li and Matsushima, 2024). Ice distribution during melting may not perfectly match that during freezing, especially if drainage pathways, air

entrapment, or dilation effects differ. Such hysteresis could influence acoustic properties and should be tested in future experiments.

Finally, fresh and saline water may coexist in natural permafrost. Although salinity has minimal effect on compressional velocity and no measurable effect on attenuation (Jones et al., 1998; Toksöz et al., 1979), it lowers the freezing point and thereby influences ice formation within the porous medium. This effect becomes particularly significant near full ice saturation, where salinity can lead to a more gradual velocity change (Lyu et al., 2020). These limitations open future research directions towards enhancing real-time monitoring of permafrost environments, which include repeating tests on different sediment types, measuring complementary parameters for a more thorough understanding of the freezing point, and upscaling laboratory results into real case in-field scenarios.

9CONCLUSION

An acoustic pulse tube was used to investigate the effect of ice content on velocity and attenuation in ice-bearing sands during melting, across a frequency range of 1–20 kHz, at three effective pressures (2.5, 5.0 & 7.5 MPa). The results serve as an analog for permafrost conditions at depths between approximately 150 and 450 m.

Ice content significantly affects the acoustic properties of the sediment. Velocity decrease occurs at all pressures, with the largest change observed at the lowest effective pressure (2.5 MPa), where weaker grain-to-grain contact allows ice to exert greater influence on the acoustic response. Additionally, attenuation increases as the ice melts, peaking at lower saturations under lower pressures and at higher saturations under higher pressures. This extension of findings further highlights the relationship between effective pressure and the acoustic behavior of ice-bearing sediments.

Both velocity and attenuation exhibit non-linear behavior with changes in ice content. Their correlation suggests that combining both parameters could potentially be used to infer ice content

at given depths within the effective pressure range of 2.5 - 7.5 MPa. Comparison with Biot three-phase models indicates that ice distribution significantly affects velocity, while attenuation is more influenced by pore structure, reflecting ice morphologies (the proportion of pore-filling to cementing ice) and the sediment frame's permeability, as well as pressure conditions.

Compared to studies at ultrasonic frequencies, the lower-frequency measurements used in this study provide insights at scales relevant to field applications. These findings highlight the importance of understanding ice saturation, distribution, and morphology for accurately predicting acoustic wave behavior in ice-bearing sediments, with potential applications for permafrost monitoring.

DATA AND MATERIALS AVAILABILITY

Data associated with this research are available and can be accessed via the following URL: https://doi.org/10.5258/SOTON/D3398.

APPENDICES

Appendix A. Sample preparation

The samples were prepared by pouring sand into the PVC pipe and compacting it layer by layer. Both ends of the pipe were sealed with PVC caps (Figure A.1), which had rubber O-rings that maintained a seal while allowing the surrounding fluid (water) to apply even hydrostatic pressure on the sand. The top of each layer was lightly scratched to avoid impedance differences between layers. The process was repeated until the pipe was fully compacted, leaving room for the top cap. We saturated the sand by gradually introducing de-ionized water, increasing saturation in steps by around 10%. To remove air bubbles during saturation, the pipe was tapped continuously. Once saturation was achieved, the top cap was sealed, and the sample was left for 24 hours before the water-saturated pulse tube measurement. Uncertainty of the sample's porosity was calculated using error propagation methods. We measured empirical porosity (ϕ) using the wet-dry mass method and compared it with theoretical porosity (ϕ_T) based on bulk dry (ρ_b) and grain (ρ_s) densities, using the formula $\phi_T = 1 - \rho_b / \rho_s$. This approach helped the assessment of uncertainties related to the saturation process due to non-connected porosity, leading to ice saturation errors of ~7%.

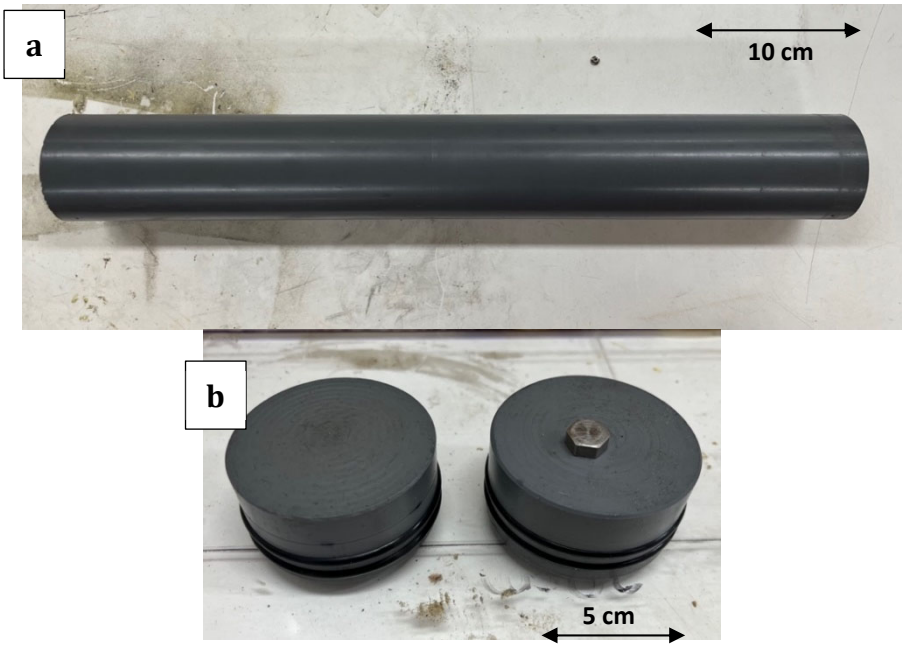

Figure A.1 *PVC jacket system used to enable sample emplacement inside the water-filled acoustic pulse tube: a) 50 cm length PVC cylinder jacket, and b) top and bottom PVC endcaps with O-ring seals, including the location of the pore fluid vent port (shown as a hexagonal nut on the top endcap on the right).*

Appendix B. Inferring ice saturation and additional rock physic modeling results

We first established a baseline by measuring the velocity and attenuation of the sample in its fully melted state ($S_i = 0$) to serve as a comparison for the measurements taken during the melting process. At the start, we assumed an initial ice saturation ($S_i = 1$) when the sample was placed in the pulse tube, though some unfrozen water likely remained, such as thin water films bound to the grains (Watanabe and Mizoguchi, 2002). However, due to the time needed to reach the target pressure in the pulse tube, measurements at full ice saturation ($S_i = 1$) were not possible, as some melting had already occurred. Instead, we used a regression model to estimate velocity and attenuation at full saturation.

We estimated ice saturation based on the melting time during the measurements, applying an empirical relationship (Equation B.1):

$$S_i = 1 - \left(\frac{t}{T}\right)^n, \tag{B.1}$$

where S_i represents ice saturation, t is the time elapsed during measurement (in seconds), T is the total time for complete melting (determined by the velocity and attenuation at the fully melted state), and n is an empirical parameter describing the exponential relationship between ice melting and time. We derived the value of n by comparing experimental results with three-phase rock physics models (Leclaire et al., 1994; Marín-Moreno et al., 2017) using visual comparison and by minimizing the objective function (Equation B.2). The function performs well when velocity and attenuation show similar variations, as in the current dataset. However, if their variation magnitudes differ significantly, one parameter may dominate the objective function. Thus, the method is most effective when both parameters vary comparably.

$$Objective\ function = \frac{|V_{experimental} - V_{modelled}|}{V_{experimental}} + \frac{|Q^{-1}_{experimental} - Q^{-1}_{modelled}|}{Q^{-1}_{experimental}} \quad \text{(B.2)}$$

Figure B.1 illustrates the closest fit between the measured and calculated velocity and attenuation, while Table B.1 provides the objective function outcomes. To determine the empirical parameter n, we considered two factors: the best fit between experimental data and model predictions using the objective function (Equation B.2), and how well the predicted experimental values at S_i = 1 (from regression models) matched the model results. We found that experimental velocity matched the models best when *n* was 1.2, 1.3, and 1.5 for the 2.5, 5, and 7.5 MPa datasets, respectively. While velocity comparisons are straightforward, the attenuation data required the objective function to better determine the *n* value.

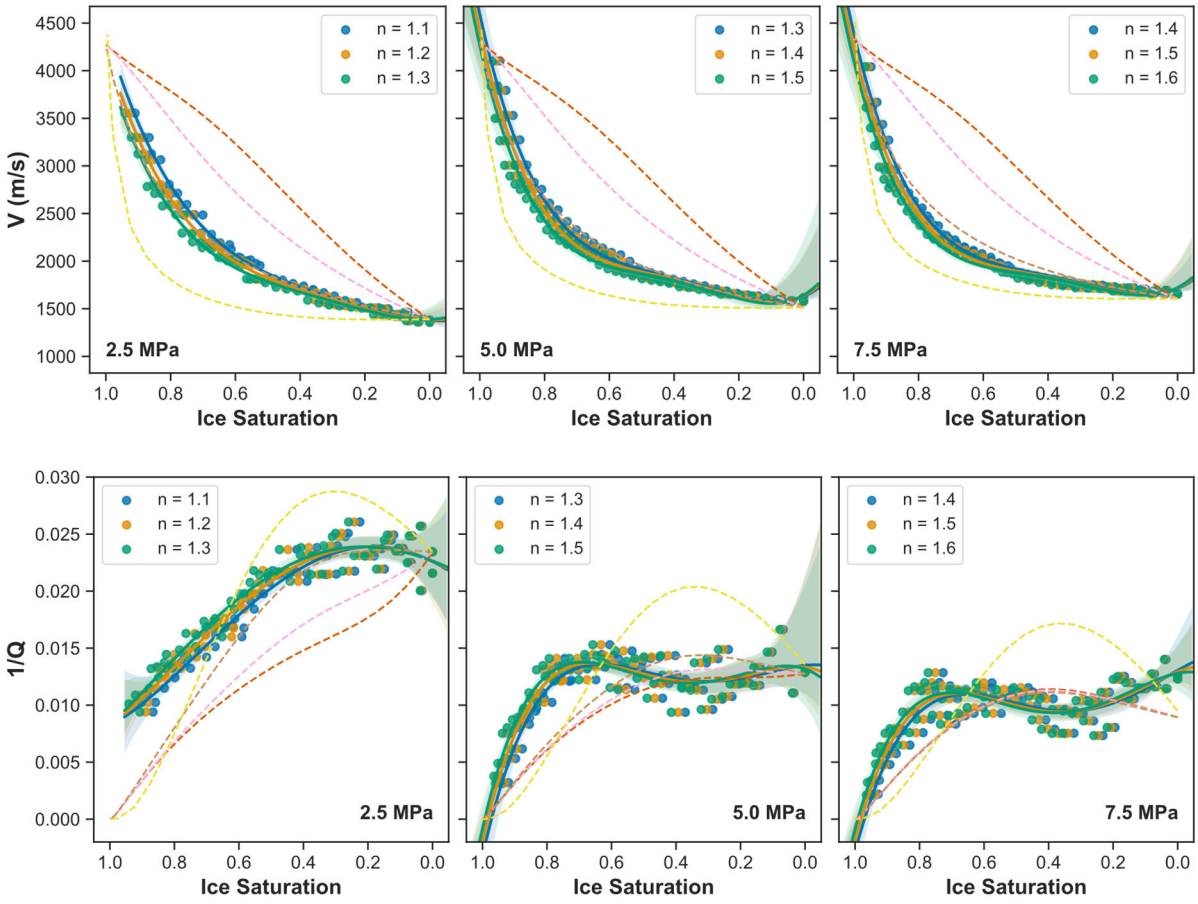

Figure B.1 *Empirical parameter (n) fitting of measured data at 10 kHz (indicated by the legend) of velocity (top) and attenuation (bottom) to HBES with Reuss, Brie, and Voigt approximations (red, pink, and brown dashed lines, respectively) and LeClaire (yellow dashed lines) models. Blue, orange, and green lines represent the respective regression models for each dataset, with an averaged R^2 of 0.98 and 0.85 for velocity and attenuation, respectively.*

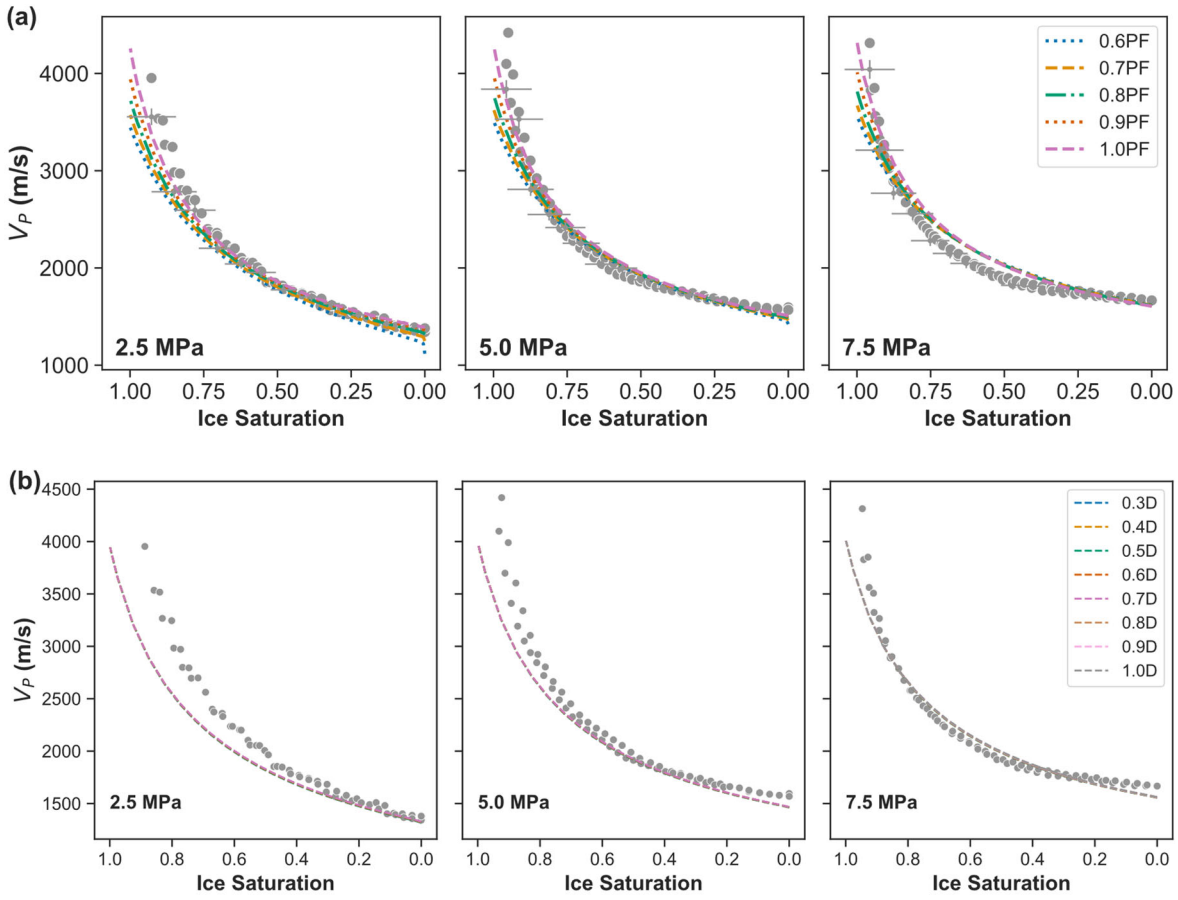

Figure B.2 *Comparison of experimental (data points) and modeled velocities (dashed lines): a) at various pore-filling (PF) saturation of ice, and b) at various permeabilities (in Darcies [D] = 1 x 10 $^{-12}$ m^2) for PF = 1.0, using the HBES model with Voigt approximations.*

Table B.1 *Calculation of objective functions to compare experimental and modelled velocity and attenuation. Best fits are indicated by lowest values (underlined).*

Dataset	**Objective function at *n* =**				
	1.1	**1.2**	**1.3**	**1.4**	**1.5**
2.5 MPa	0.359	0.349	0.351	0.359	0.375
5 MPa	0.317	0.416	0.314	0.403	0.333
7.5 MPa	0.721	0.655	0.596	0.531	0.467

REFERENCES

Abbasi, M., Mousavi, S.M., Lee, B.J., Esfahani, J.A., Karimi, N., Mamaghani, M.Y., 2022. Examination of the effects of porosity upon intensification of thermal storage of PCMs in a shell-and-tube type system. Case Stud. Therm. Eng. 33, 101963. https://doi.org/10.1016/j.csite.2022.101963

Alkire, B.D., Andersland, O.B., 1973. The Effect of Confining Pressure on the Mechanical Properties of Sand–Ice Materials. J. Glaciol. 12, 469–481. https://doi.org/10.3189/S0022143000031889

Allmark, C., Curtis, A., Galetti, E., De Ridder, S., 2018. Seismic Attenuation From Ambient Noise Across the North Sea Ekofisk Permanent Array. J. Geophys. Res. Solid Earth 123, 8691–8710. https://doi.org/10.1029/2017JB015419

Berryman, J.G., 1981. Elastic wave propagation in fluid-saturated porous media II. J. Acoust. Soc. Am. 70, 1754–1756. https://doi.org/10.1121/1.387193

Best, A.I., Priest, J.A., Clayton, C.R.I., Rees, E.V.L., 2013. The effect of methane hydrate morphology and water saturation on seismic wave attenuation in sand under shallow sub-seafloor conditions. Earth Planet. Sci. Lett. 368, 78–87. https://doi.org/10.1016/j.epsl.2013.02.033

Biot, M.A., 1956a. Theory of Propagation of Elastic Waves in a Fluid-Saturated Porous Solid. I. Low-Frequency Range. J. Acoust. Soc. Am. 28, 168–178. https://doi.org/10.1121/1.1908239

Biot, M.A., 1956b. Theory of Propagation of Elastic Waves in a Fluid-Saturated Porous Solid. II. Higher Frequency Range. J. Acoust. Soc. Am. 28, 179–191. https://doi.org/10.1121/1.1908241

Brie, A., Pampuri, F., Marsala, A.F., Meazza, O., 1995. Shear Sonic Interpretation in Gas-Bearing Sands. Presented at the SPE Annual Technical Conference and Exhibition, p. SPE-30595-MS. https://doi.org/10.2118/30595-MS

Bustamante, J., Fabien-Ouellet, G., Duchesne, M.J., Ibrahim, A., 2023. Understanding seismic velocity variations of subsea permafrost: A sensitivity study. Geophysics R655–R669. https://doi.org/10.1190/geo2022-0568.1

Carcione, J.M., Helle, H.B., Pham, N.H., 2003. White's model for wave propagation in partially saturated rocks: Comparison with poroelastic numerical experiments. GEOPHYSICS 68, 1389–1398. https://doi.org/10.1190/1.1598132

Chang, X., Liu, W., Zuo, G., Dou, Y., Li, Y., 2021. Research on ultrasonic-based investigation of mechanical properties of ice. Acta Oceanol. Sin. 40, 97–105. https://doi.org/10.1007/s13131-021-1890-3

Dash, J.G., Fu, H., Wettlaufer, J.S., 1995. The premelting of ice and its environmental consequences. Rep. Prog. Phys. 58, 115–167. https://doi.org/10.1088/0034-4885/58/1/003

De Lemos, M.J.S., 2012. Applications in Hybrid Media, in: Turbulence in Porous Media. Elsevier, pp. 199–352. https://doi.org/10.1016/B978-0-08-098241-0.00011-5

Desai, K.P., Moore, E.J., 1968. Well Log Interpretation In Permafrost. Log Anal. 9.

Dobiński, W., 2020. Permafrost active layer. Earth-Sci. Rev. 208, 103301. https://doi.org/10.1016/j.earscirev.2020.103301

Dou, S., Nakagawa, S., Dreger, D., Ajo-Franklin, J., 2016. A rock-physics investigation of unconsolidated saline permafrost: P-wave properties from laboratory ultrasonic

measurements. Geophysics 81, WA233–WA245. https://doi.org/10.1190/geo2015-0176.1

Dvorkin, J., Prasad, M., Sakai, A., Lavoie, D., 1999. Elasticity of marine sediments: Rock physics modeling. Geophys. Res. Lett. 26, 1781–1784. https://doi.org/10.1029/1999GL900332

Ecker, C., Dvorkin, J., Nur, A., 1998. Sediments with gas hydrates: Internal structure from seismic AVO. Geophysics 63, 1659–1669.

Ecker, C., Dvorkin, J., Nur, A.M., 2000. Estimating the amount of gas hydrate and free gas from marine seismic data. Geophysics 65, 565–573. https://doi.org/10.1190/1.1444752

Emerson, M., Foray, P., 2006. Laboratory P-wave measurements in dry and saturated sand. Acta Geotech. 1, 167–177. https://doi.org/10.1007/s11440-006-0015-7

Falcon-Suarez, I.H., Amalokwu, K., Delgado-Martin, J., Callow, B., Robert, K., North, L., Sahoo, S.K., Best, A.I., 2019. Comparison of stress-dependent geophysical, hydraulic and mechanical properties of synthetic and natural sandstones for reservoir characterization and monitoring studies. Geophys. Prospect. 67, 784–803. https://doi.org/10.1111/1365-2478.12699

French, H.M., 2007. Permafrost, in: The Periglacial Environment. pp. 83–115. https://doi.org/10.1002/9781118684931.ch5

Fuchs, M., Grosse, G., Jones, B.M., Strauss, J., Baughman, C.A., Walker, D.A., 2018. Sedimentary and geochemical characteristics of two small permafrost-dominated Arctic river deltas in northern Alaska. arktos 4, 1–18. https://doi.org/10.1007/s41063-018-0056-9

Hearst, J.R., Nelson, P.H., 1985. Well logging for physical properties. Mc Graw-Hill Book Co, United States.

Hefner, B.T., Jackson, D.R., Calantoni, J., Reed, A.H., 2006. Dispersion and attenuation due to scattering from heterogeneities in the porosity of sand sediments. J. Acoust. Soc. Am. 120, 3098–3099. https://doi.org/10.1121/1.4787533

Helgerud, M.B., Dvorkin, J., Nur, A., Sakai, A., Collett, T., 1999. Elastic-wave velocity in marine sediments with gas hydrates: Effective medium modeling. Geophys. Res. Lett. 26, 2021–2024. https://doi.org/10.1029/1999GL900421

Helgerud, M.B., Waite, W.F., Kirby, S.H., Nur, A., 2009. Elastic wave speeds and moduli in polycrystalline ice Ih, sI methane hydrate, and sII methane-ethane hydrate. J. Geophys. Res. 114, B02212. https://doi.org/10.1029/2008JB006132

Hilbich, C., Hauck, C., Mollaret, C., Wainstein, P., Arenson, L.U., 2022. Towards accurate quantification of ice content in permafrost of the Central Andes – Part 1: Geophysics-based estimates from three different regions. The Cryosphere 16, 1845–1872. https://doi.org/10.5194/tc-16-1845-2022

Hjort, J., Karjalainen, O., Aalto, J., Westermann, S., Romanovsky, V.E., Nelson, F.E., Etzelmüller, B., Luoto, M., 2018. Degrading permafrost puts Arctic infrastructure at risk by mid-century. Nat. Commun. 9, 5147. https://doi.org/10.1038/s41467-018-07557-4

Hu, G., Ye, Y., Liu, C., Best, A., Li, C., 2014. Gas hydrate distribution in sediment pore space and its impact on acoustic properties of hydrate-bearing sediments, in: Proceedings of the 8th International Conference on Gas Hydrates.

Jones, S.M., McCann, C., Astin, T.R., Sothcott, J., 1998. The effects of pore-fluid salinity on ultrasonic wave propagation in sandstones. GEOPHYSICS 63, 928–934. https://doi.org/10.1190/1.1444404

Kang, S., Jin, Y.K., Jang, U., Duchesne, M.J., Shin, C., Kim, S., Riedel, M., Dallimore, S.R., Paull, C.K., Choi, Y., Hong, J.K., 2021. Imaging the P-Wave Velocity Structure of Arctic Subsea Permafrost Using Laplace-Domain Full-Waveform Inversion. J. Geophys. Res. Earth Surf. 126, e2020JF005941. https://doi.org/10.1029/2020JF005941

Kawasaki, K., Osterkamp, T.E., Jurick, R.W., Kienle, J., 1983. Gravity Measurements in Permafrost Terrain Containing Massive Ground Ice. Ann. Glaciol. 4, 133–140. https://doi.org/10.3189/S026030550000536X

Kim, I.-W., Timmermann, A., Kim, J.-E., Rodgers, K.B., Lee, S.-S., Lee, H., Wieder, W.R., 2024. Abrupt increase in Arctic-Subarctic wildfires caused by future permafrost thaw. Nat. Commun. 15, 7868. https://doi.org/10.1038/s41467-024-51471-x

Kolsky, H., 1964. Stress waves in solids. J. Sound Vib. 1, 88–110. https://doi.org/https://doi.org/10.1016/0022-460X(64)90008-2

Leclaire, Ph., Cohen-Ténoudji, F., Aguirre-Puente, J., 1994. Extension of Biot's theory of wave propagation to frozen porous media. J. Acoust. Soc. Am. 96, 3753–3768. https://doi.org/10.1121/1.411336

Lee, J.-W., Kim, J.-S., Hong, C.-H., Oh, T.-M., 2024. Permeability monitoring of underground concrete structures using elastic wave characteristics with modified Biot's model. Sci. Rep. 14, 22110. https://doi.org/10.1038/s41598-024-73449-x

Li, B., Matsushima, J., 2024. Influence of ice properties on wave propagation characteristics in partially frozen soils and rocks: A temperature-dependent rock-physics model. Geophysics 89, MR281–MR295. https://doi.org/10.1190/geo2023-0694.1

Lin, Z., Pan, H., Fang, H., Gao, W., Liu, D., 2018. High-altitude well log evaluation of a permafrost gas hydrate reservoir in the Muli area of Qinghai, China. Sci. Rep. 8, 12596. https://doi.org/10.1038/s41598-018-30795-x

Liu, L., Zang, S., Wu, X., Liu, R., Li, T., Zhu, J., Sun, L., Wu, S., Dong, X., Zhang, Z., 2023. Sediment Grain-Size Composition in the Permafrost Region of the Greater Khingan Range and Its Significance as a Material Source. Land 12, 1728. https://doi.org/10.3390/land12091728

Lyu, C., Amiri, S.A.G., Grimstad, G., Høyland, K.V., Ingeman-Nielsen, T., 2020. Comparison of Geoacoustic Models for Unfrozen Water Content Estimation. J. Geophys. Res. Solid Earth 125, e2020JB019766. https://doi.org/10.1029/2020JB019766

Mahabadi, N., Dai, S., Seol, Y., Jang, J., 2019. Impact of hydrate saturation on water permeability in hydrate-bearing sediments. J. Pet. Sci. Eng. 174, 696–703. https://doi.org/10.1016/j.petrol.2018.11.084

Marín-Moreno, H., Sahoo, S.K., Best, A.I., 2017. Theoretical modeling insights into elastic wave attenuation mechanisms in marine sediments with pore-filling methane hydrate: Hydrate-Bearing Effective Sediment Model. J. Geophys. Res. Solid Earth. https://doi.org/10.1002/2016JB013577

Matsushima, J., Suzuki, M., Kato, Y., Rokugawa, S., 2016. Ultrasonic measurements of attenuation and velocity of compressional and shear waves in partially frozen unconsolidated sediment and synthetic porous rock. Geophysics 81, D141–D153. https://doi.org/10.1190/geo2015-0350.1

Mavko, G., Mukerji, T., Dvorkin, J., 2009. The Rock Physics Handbook, 2nd ed. Cambridge University Press.

McCann, C., Sothcott, J., Best, A.I., 2014. A new laboratory technique for determining the compressional wave properties of marine sediments at sonic frequencies and *in situ* pressures: Compressional wave properties of marine sediments. Geophys. Prospect. 62, 97–116. https://doi.org/10.1111/1365-2478.12079

McCutchan, A., Johnson, B., 2022. Laboratory Experiments on Ice Melting: A Need for Understanding Dynamics at the Ice-Water Interface. J. Mar. Sci. Eng. 10, 1008. https://doi.org/10.3390/jmse10081008

Meredith, M., Sommerkorn, M., Casotta, S., Derksen, C., Ekaykin, A., Hollowed, A., Kofinas, G., Mackintosh, A., Melbourne-Thomas, J., Muelbert, M., Ottersen, G., Pritchard, H., Schuur, E., 2022. The Ocean and Cryosphere in a Changing Climate: Special Report of the Intergovernmental Panel on Climate Change, 1st ed. Cambridge University Press. https://doi.org/10.1017/9781009157964

Mindlin, R.D., 1949. Compliance of Elastic Bodies in Contact. J. Appl. Mech. 16, 259–268. https://doi.org/10.1115/1.4009973

Mobley, J., Waters, K.R., Hughes, M.S., Hall, C.S., Marsh, J.N., Brandenburger, G.H., Miller, J.G., 2000. Kramers–Kronig relations applied to finite bandwidth data from suspensions of encapsulated microbubbles. J. Acoust. Soc. Am. 108, 2091–2106. https://doi.org/10.1121/1.1312364

Müller, T.M., Gurevich, B., Lebedev, M., 2010. Seismic wave attenuation and dispersion resulting from wave-induced flow in porous rocks — A review. Geophysics 75. https://doi.org/10.1190/1.3463417

Murphy, W.F., 1982. Effects of Microstructure and Pore Fluids on the Acoustic Properties of Granular Sedimentary Materials, Stanford Rock Physics Project report. Stanford University.

Nakano, Y., Arnold, R., 1973. Acoustic properties of frozen Ottawa sand. Water Resour. Res. 9, 178–184. https://doi.org/10.1029/WR009i001p00178

North, L., Best, A., 2015. An Improved High-Spectral Resolution Water Filled Impedance Tube Measurement Method For Marine Sediment Studies, in: Seabed and Sediment Acoustics 2015. Presented at the Seabed and Sediment Acoustics 2015, Institute of Acoustics, Bath. https://doi.org/10.25144/18070

Osterkamp, T.E., Payne, M.W., 1981. Estimates of permafrost thickness from well logs in northern Alaska. Cold Reg. Sci. Technol. 5, 13–27. https://doi.org/10.1016/0165-232X(81)90037-9

Oswell, J.M., 2011. Pipelines in permafrost: geotechnical issues and lessons [1] 2010 R.M. Hardy Address, 63rd Canadian Geotechnical Conference. Can. Geotech. J. 48, 1412–1431. https://doi.org/10.1139/t11-045

Parolai, S., Lai, C.G., Dreossi, I., Ktenidou, O.-J., Yong, A., 2022. A review of near-surface QS estimation methods using active and passive sources. J. Seismol. 26, 823–862. https://doi.org/10.1007/s10950-021-10066-5

Priest, J.A., Abbas, M., Hayley, J.L., 2021. The Change in Geomechanical Properties of Gas Saturated Methane Hydrate-Bearing Sand Resulting From Water Saturation. J. Geophys. Res. Solid Earth 126. https://doi.org/10.1029/2021JB022245

Priest, J.A., Rees, E.V.L., Clayton, C.R.I., 2009. Influence of gas hydrate morphology on the seismic velocities of sands. J. Geophys. Res. Solid Earth 114, 2009JB006284. https://doi.org/10.1029/2009JB006284

Redwood, Martin., 1960. Mechanical waveguides; the propagation of acoustic and ultrasonic waves in fluids and solids with boundaries. Pergamon Press, New York.

Reuss, A., 1929. Berechnung der Fließgrenze von Mischkristallen auf Grund der Plastizitätsbedingung für Einkristalle . ZAMM - Z. Für Angew. Math. Mech. 9, 49–58. https://doi.org/10.1002/zamm.19290090104

Rubino, J.G., Holliger, K., 2012. Seismic attenuation and velocity dispersion in heterogeneous partially saturated porous rocks: Mesoscopic effects and partial saturation. Geophys. J. Int. 188, 1088–1102. https://doi.org/10.1111/j.1365-246X.2011.05291.x

Sahoo, S.K., Best, A.I., 2021. The Influence of Gas Hydrate Morphology on Reservoir Permeability and Geophysical Shear Wave Remote Sensing. J. Geophys. Res. Solid Earth 126. https://doi.org/10.1029/2021JB022206

Sahoo, S.K., Madhusudhan, B.N., Marín-Moreno, H., North, L.J., Ahmed, S., Falcon-Suarez, I.H., Minshull, T.A., Best, A.I., 2018. Laboratory Insights Into the Effect of Sediment-Hosted Methane Hydrate Morphology on Elastic Wave Velocity From Time-Lapse 4-D Synchrotron X-Ray Computed Tomography. Geochem. Geophys. Geosystems 19, 4502–4521. https://doi.org/10.1029/2018GC007710

Schumann, K., Stipp, M., Behrmann, J.H., Klaeschen, D., Schulte-Kortnack, D., 2014. *P* and *S* wave velocity measurements of water-rich sediments from the Nankai Trough, Japan: P- and S-wave velocity measurements. J. Geophys. Res. Solid Earth 119, 787–805. https://doi.org/10.1002/2013JB010290

Schuur, E.A.G., McGuire, A.D., Schädel, C., Grosse, G., Harden, J.W., Hayes, D.J., Hugelius, G., Koven, C.D., Kuhry, P., Lawrence, D.M., Natali, S.M., Olefeldt, D., Romanovsky, V.E., Schaefer, K., Turetsky, M.R., Treat, C.C., Vonk, J.E., 2015. Climate change and the permafrost carbon feedback. Nature 520, 171–179. https://doi.org/10.1038/nature14338

Selfridge, A.R., 1985. Approximate Material Properties in Isotropic Materials. IEEE Trans. Sonics Ultrason. 32, 381–394. https://doi.org/10.1109/T-SU.1985.31608

Simmons, G., 1965. Single Crystal Elastic Constants and Calculated Aggregate Properties 274.

Sizemore, H.G., Mellon, M.T., 2008. Laboratory characterization of the structural properties controlling dynamical gas transport in Mars-analog soils. Icarus 197, 606–620. https://doi.org/10.1016/j.icarus.2008.05.013

Snehota, M., Jelinkova, V., Sobotkova, M., Sacha, J., Vontobel, P., Hovind, J., 2015. Water and entrapped air redistribution in heterogeneous sand sample: Quantitative neutron imaging of the process. Water Resour. Res. 51, 1359–1371. https://doi.org/10.1002/2014WR015432

Spangenberg, E., Seyberth, K., Heeschen, K.U., Priegnitz, M., Schicks, J.M., 2018. A *Quick Look* Method to Assess the Dependencies of Rock Physical Sediment Properties on the Saturation With Pore-Filling Hydrate. J. Geophys. Res. Solid Earth 123, 5588–5598. https://doi.org/10.1029/2018JB015855

Strauss, J., Schirrmeister, L., Wetterich, S., Borchers, A., Davydov, S.P., 2012. Grain-size properties and organic-carbon stock of Yedoma Ice Complex permafrost from the

Kolyma lowland, northeastern Siberia. Glob. Biogeochem. Cycles 26, 2011GB004104. https://doi.org/10.1029/2011GB004104

Sutiyoso, H.S., 2025. A Laboratory Acoustic Study of Fluid and Ice Saturation Effects in Sands. University of Southampton, Southampton.

Sutiyoso, H.S., Sahoo, S.K., North, L.J., Falcon-Suarez, I.H., Minshull, T.A., Best, A.I., 2025. Laboratory Measurement of Sonic (1–20 kHz) P-Wave Velocity and Attenuation During Melting of Ice-Bearing Sand. J. Geophys. Res. Solid Earth 130, e2024JB030465. https://doi.org/10.1029/2024JB030465

Sutiyoso, H.S., Sahoo, S.K., North, L.J., Minshull, T.A., Falcon-Suarez, I.H., Best, A.I., 2024. Laboratory measurements of water saturation effects on the acoustic velocity and attenuation of sand packs in the 1–20 kHz frequency range. Geophys. Prospect. https://doi.org/10.1111/1365-2478.13607

Toksöz, M.N., Johnston, D.H., Timur, A., 1979. Attenuation of seismic waves in dry and saturated rocks: I. Laboratory measurements. Geophysics 44, 681–690. https://doi.org/10.1190/1.1440969

Voigt, W., 1889. Ueber die Beziehung zwischen den beiden Elasticitätsconstanten isotroper Körper. Ann. Phys. 274, 573–587. https://doi.org/10.1002/andp.18892741206

Wagner, W., Riethmann, T., Feistel, R., Harvey, A.H., 2011. New Equations for the Sublimation Pressure and Melting Pressure of H2O Ice Ih. J. Phys. Chem. Ref. Data 40, 043103. https://doi.org/10.1063/1.3657937

Watanabe, K., Mizoguchi, M., 2002. Amount of unfrozen water in frozen porous media saturated with solution. Cold Reg. Sci. Technol. 34, 103–110. https://doi.org/10.1016/S0165-232X(01)00063-5

Wu, R., Aki, K., 1985. Scattering characteristics of elastic waves by an elastic heterogeneity. GEOPHYSICS 50, 582–595. https://doi.org/10.1190/1.1441934

Yang, L., Jia, H., Han, L., Zhang, H., Tang, L., 2021. Hysteresis in the ultrasonic parameters of saturated sandstone during freezing and thawing and correlations with unfrozen water content. J. Rock Mech. Geotech. Eng. 13, 1078–1092. https://doi.org/10.1016/j.jrmge.2021.06.006

Zimmer, M., 2003. Seismic velocities in unconsolidated sands: measurements of pressure, sorting and compaction effects.

Zimmer, M., Prasad, M., Mavko, G., 2002. Pressure and porosity influences on VP–VS ratio in unconsolidated sands. Lead. Edge 21, 178–183. https://doi.org/10.1190/1.1452609

LIST OF FIGURES

Figure 1 Comparison of compressional velocity (V_P) of water-saturated sand measured in this study with values reported in published studies. The three data points for this study represent measurements at different effective pressures (2.5, 5.0, and 7.5 MPa), with error bars indicating experimental uncertainty. Marker size represents the confining pressure, ranging from atmospheric pressure to 10 MPa. The study codes are as follows: KG (Kang et al., 2021), YG (Yang et al., 2021), SP (Spangenberg et al., 2018), DOU (Dou et al., 2016), and NAKA (Nakano and Arnold, 1973). 9

Figure 2 Experimental apparatus and resulting raw and processed data: (a) Schematic diagram of the pulse tube with dimensions; (b) details of the PVC-jacketed sample inside the water-filled pulse tube; (c) raw time-series signals acquired during measurements; (d) deconvolved signals for water-saturated and ice-bearing sand samples on both hydrophones (see panel (a) for hydrophone positions). 10

Figure 3 Variations in P-wave velocity (V_P) and attenuation ($1/Q_P$) at 10 kHz during the ice melting process at various effective pressures, with shaded areas representing fourth-order polynomial regression models with a confidence interval of 90% (R^2 of 0.99, 0.98, 0.98 for velocity and 0.94, 0.82, 0.79 for attenuation at 2.5, 5, and 7.5 MPa, respectively). Error bars are plotted every 10 data points. 14

Figure 4 Experimental results: a) P-wave velocity (V_P) and b) attenuation ($1/Q_P$) spectra at selected ice saturations (S_i). The error bars are smaller than the symbol sizes. Legends represent effective pressures in megapascals (MPa). 16

Figure 5 Regression slope of P-wave velocity (V_P) versus frequency between the cut-off and maximum (20 kHz) frequencies as a function of ice saturations and effective pressures. Positive slopes indicate velocity increasing with frequency, while negative slopes indicate velocity decreasing with frequency. Legends represent effective pressures in megapascals (MPa). 16

Figure 6 Spearman's rank correlation coefficients between acoustic properties (P-wave velocity, V_P and attenuation, $1/Q_P$) and ice saturation, calculated at each frequency and effective pressure (in megapascals). The vertical axis ranges from -1 to +1 to accommodate both positive (typically for velocity) and negative (typically for attenuation) correlations. The 90% and 99% confidence level lines apply to both acoustic properties and indicate statistically significant correlations.... 18

Figure 7 Comparison of experimental data and model results for P-waves at 10 kHz: a) velocity (V_P) and b) attenuation ($1/Q_P$). In the HBES models, the pore-filling saturation PF is 1.0 and the permeability is 0.5 D; c) attenuation at different PF (with the remainder of S_i as cementing ice, i.e., 1 - PF); and d) attenuation at different permeabilities for PF = 1.0. Results in c) and d) are modeled using the HBES model with Voigt approximation. Cross-error bars are plotted every 15 experimental data points. 21

Figure 8 Variations in P-wave velocity (V_P) and attenuation ($1/Q_P$) at 10 kHz plotted against each other, with lines representing second-order polynomial regression models with R^2 of 0.94, 0.72, and 0.72 at 2.5, 5, and 7.5 MPa, respectively. Marker types represent different effective pressures as shown in the legend. Cross-error bars are plotted every 15 data points. 25

Figure A.1 PVC jacket system used to enable sample emplacement inside the water-filled acoustic pulse tube: a) 50 cm length PVC cylinder jacket, and b) top and bottom PVC endcaps with O-ring seals, including the location of the pore fluid vent port (shown as a hexagonal nut on the top endcap on the right). ..... **Error! Bookmark not defined.**

Figure B.1 Empirical parameter (n) fitting of measured data at 10 kHz (indicated by the legend) of velocity (top) and attenuation (bottom) to HBES with Reuss, Brie, and Voigt approximations (red, pink, and brown dashed lines, respectively) and LeClaire (yellow dashed lines) models. Blue, orange, and green lines represent the respective regression models for each dataset with an averaged R^2 of 0.98 and 0.85 for velocity and attenuation, respectively. 31

Figure B.2 Comparison of experimental and modelled velocities: a) at various pore-filling (PF) saturation of ice, and b) at various permeabilities (in Darcies [D] = 1 x 10^{-12} m²) for PF = 1.0, using the HBES model with Voigt approximations. 32

LIST OF TABLES

Table 1 Fixed and case-dependent input parameters used in the model runs (case-dependent parameters are used only in HBES model runs). 11

Table B.1 Calculation of objective functions to compare experimental and modelled velocity and attenuation. Best fits are indicated by lowest values (underlined). 32

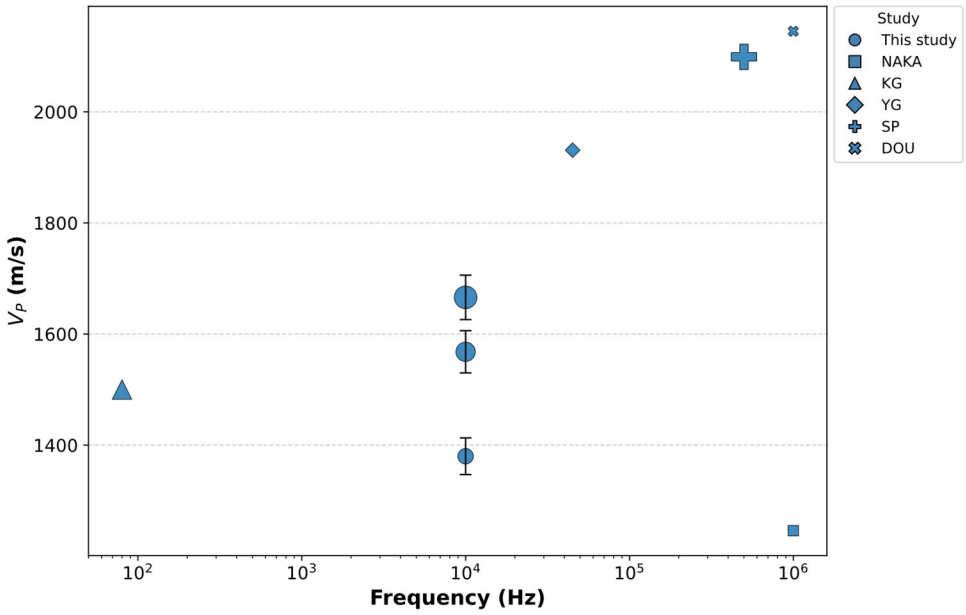

Figure 1 Comparison of compressional velocity (V_P) of water-saturated sand measured in this study with values reported in published studies. The three data points for this study represent measurements at different effective pressures (2.5, 5.0, and 7.5 MPa), with error bars indicating experimental uncertainty. Marker size represents the confining pressure, ranging from atmospheric pressure to 10 MPa. The study codes are as follows: KG (Kang et al., 2021), YG (Yang et al., 2021), SP (Spangenberg et al., 2018), DOU (Dou et al., 2016), and NAKA (Nakano and Arnold, 1973).
1301x829mm (400 x 400 DPI)

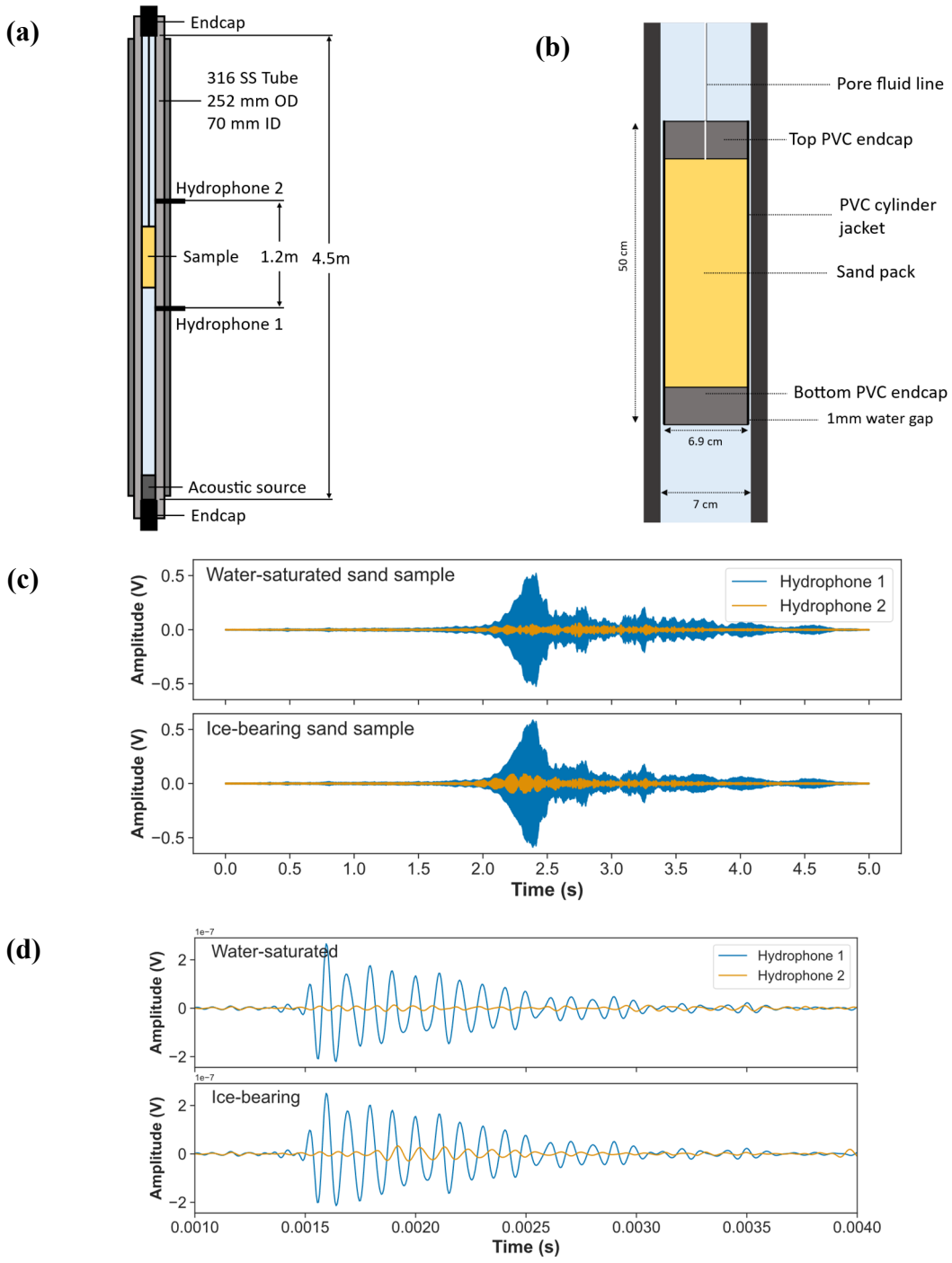

Figure 2 Experimental apparatus and resulting raw and processed data: (a) Schematic diagram of the pulse tube with dimensions; (b) details of the PVC-jacketed sample inside the water-filled pulse tube; (c) raw time-series signals acquired during measurements; (d)

deconvolved signals for water-saturated and ice-bearing sand samples on both hydrophones (see panel (a) for hydrophone positions).

664x1010mm (330 x 330 DPI)

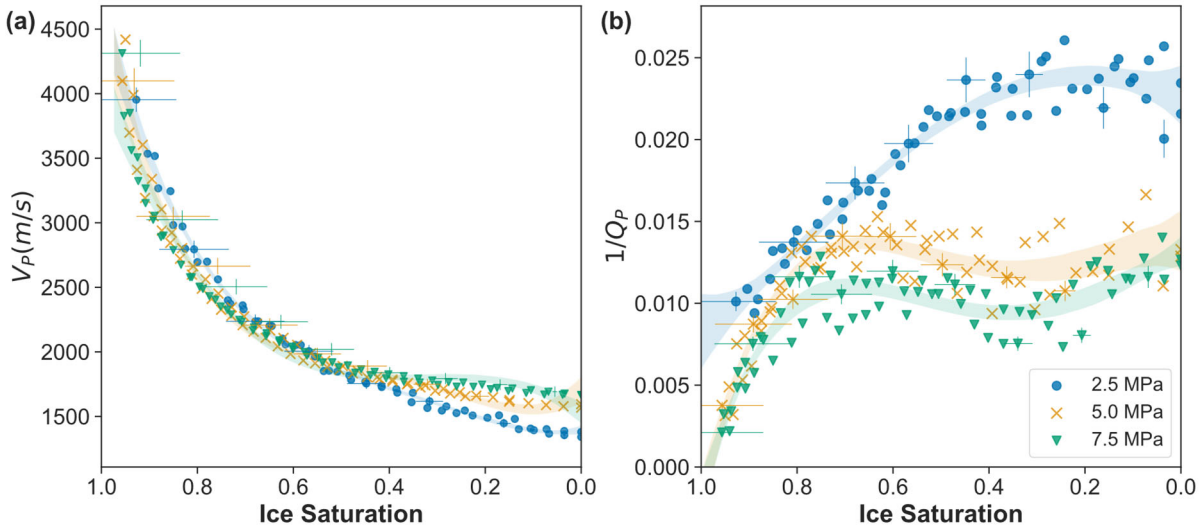

Figure 3 Variations in P-wave velocity (V_P) and attenuation ($1/Q_P$) at 10 kHz during the ice melting process at various effective pressures, with shaded areas representing fourth-order polynomial regression models with a confidence interval of 90% (R^2 of 0.99, 0.98, 0.98 for velocity and 0.94, 0.82, 0.79 for attenuation at 2.5, 5, and 7.5 MPa, respectively). Error bars are plotted every 10 data points.
1716x765mm (400 x 400 DPI)

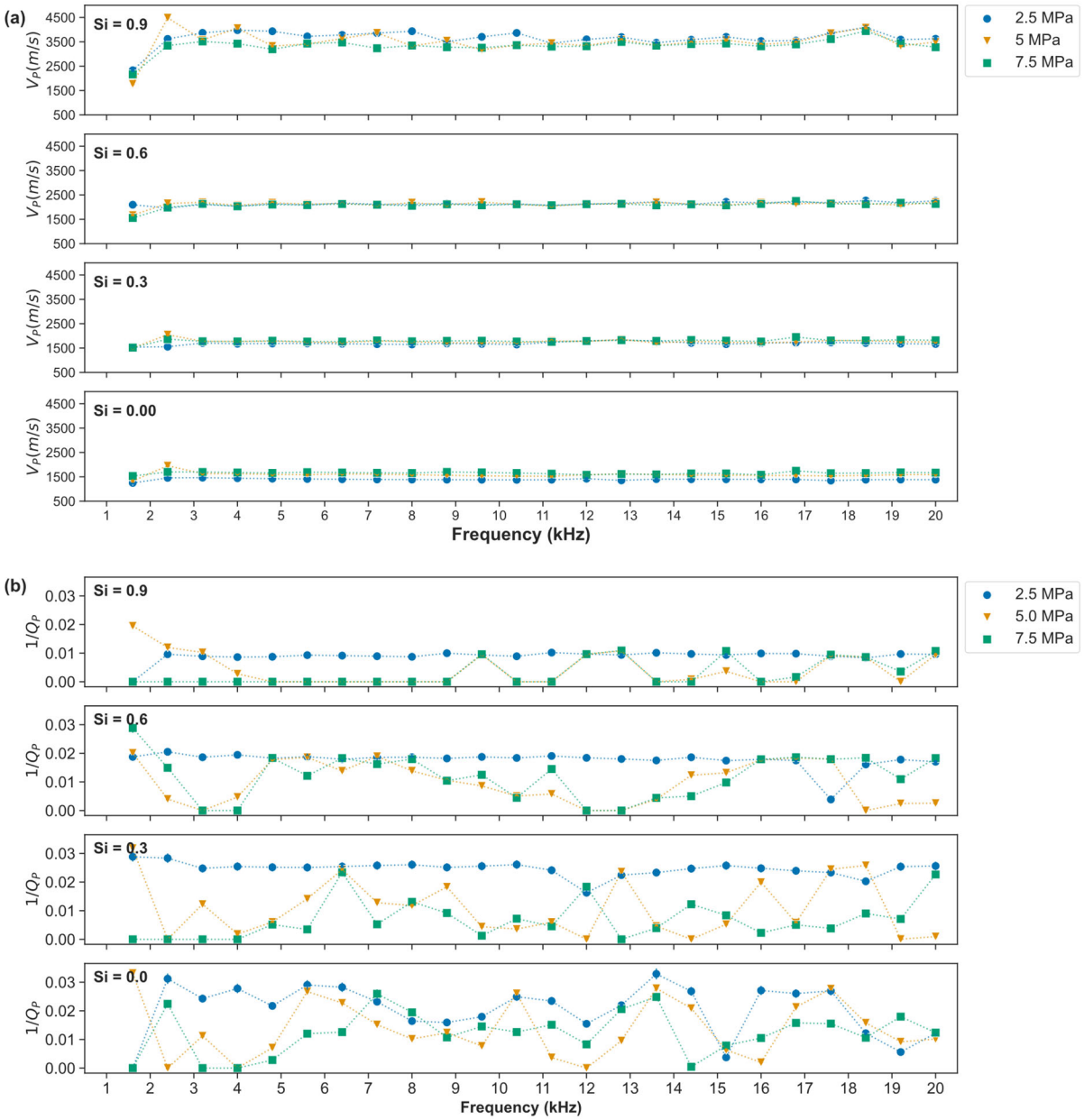

Figure 4 Experimental results: a) P-wave velocity (V_P) and b) attenuation ($1/Q_P$) spectra at selected ice saturations (S_i). The error bars are smaller than the symbol sizes. Legends represent effective pressures in megapascals (MPa).
873x887mm (330 x 330 DPI)

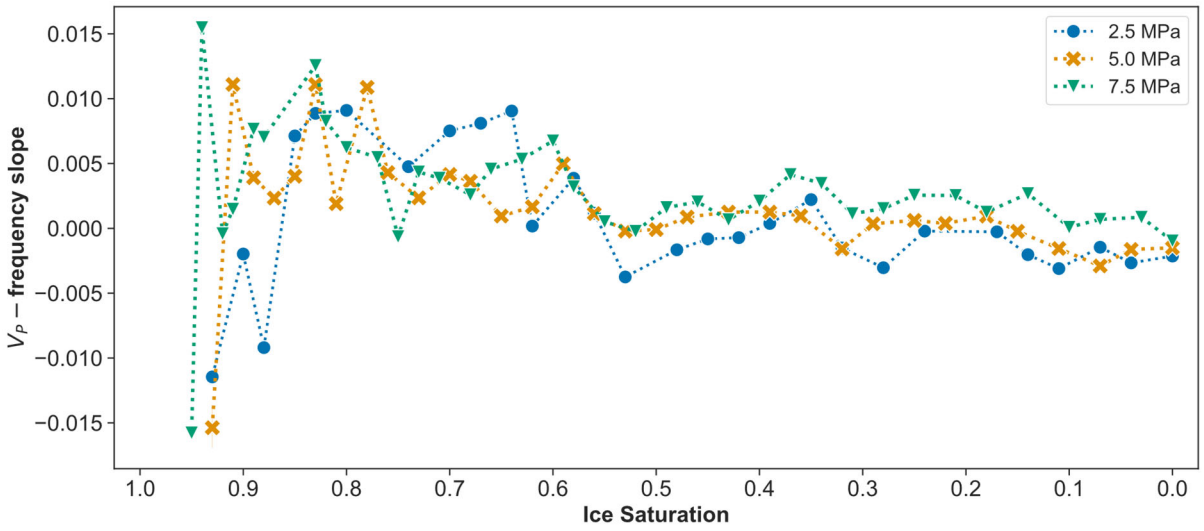

Figure 5 Regression slope of P-wave velocity (V_P) versus frequency between the cut-off and maximum (20 kHz) frequencies as a function of ice saturations and effective pressures. Positive slopes indicate velocity increasing with frequency, while negative slopes indicate velocity decreasing with frequency. Legends represent effective pressures in megapascals (MPa).
1710x760mm (400 x 400 DPI)

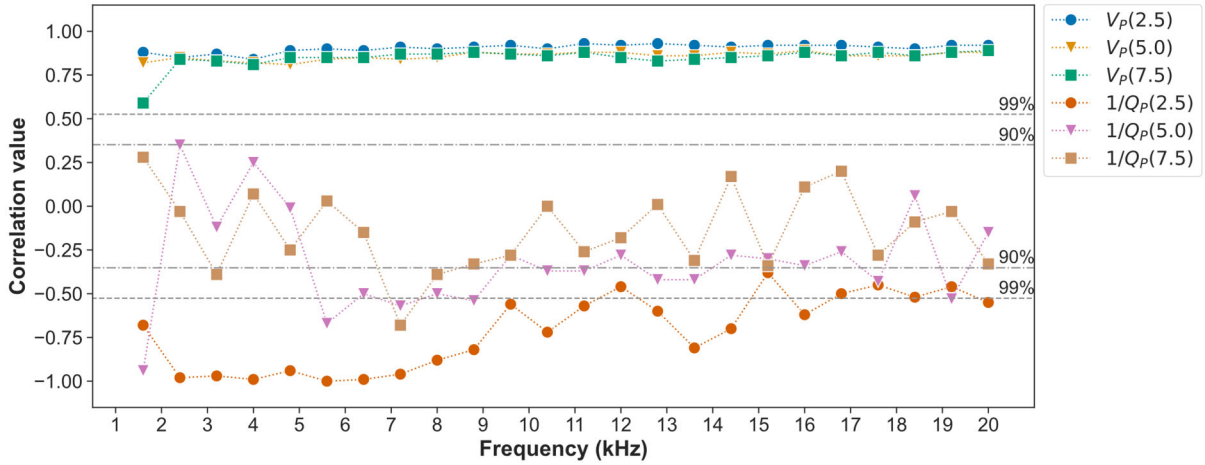

Figure 6 Spearman's rank correlation coefficients between acoustic properties (P-wave velocity, V_P and attenuation, $1/Q_P$) and ice saturation, calculated at each frequency and effective pressure (in megapascals). The vertical axis ranges from -1 to +1 to accommodate both positive (typically for velocity) and negative (typically for attenuation) correlations. The 90% and 99% confidence level lines apply to both acoustic properties and indicate statistically significant correlations.

1965x766mm (400 x 400 DPI)

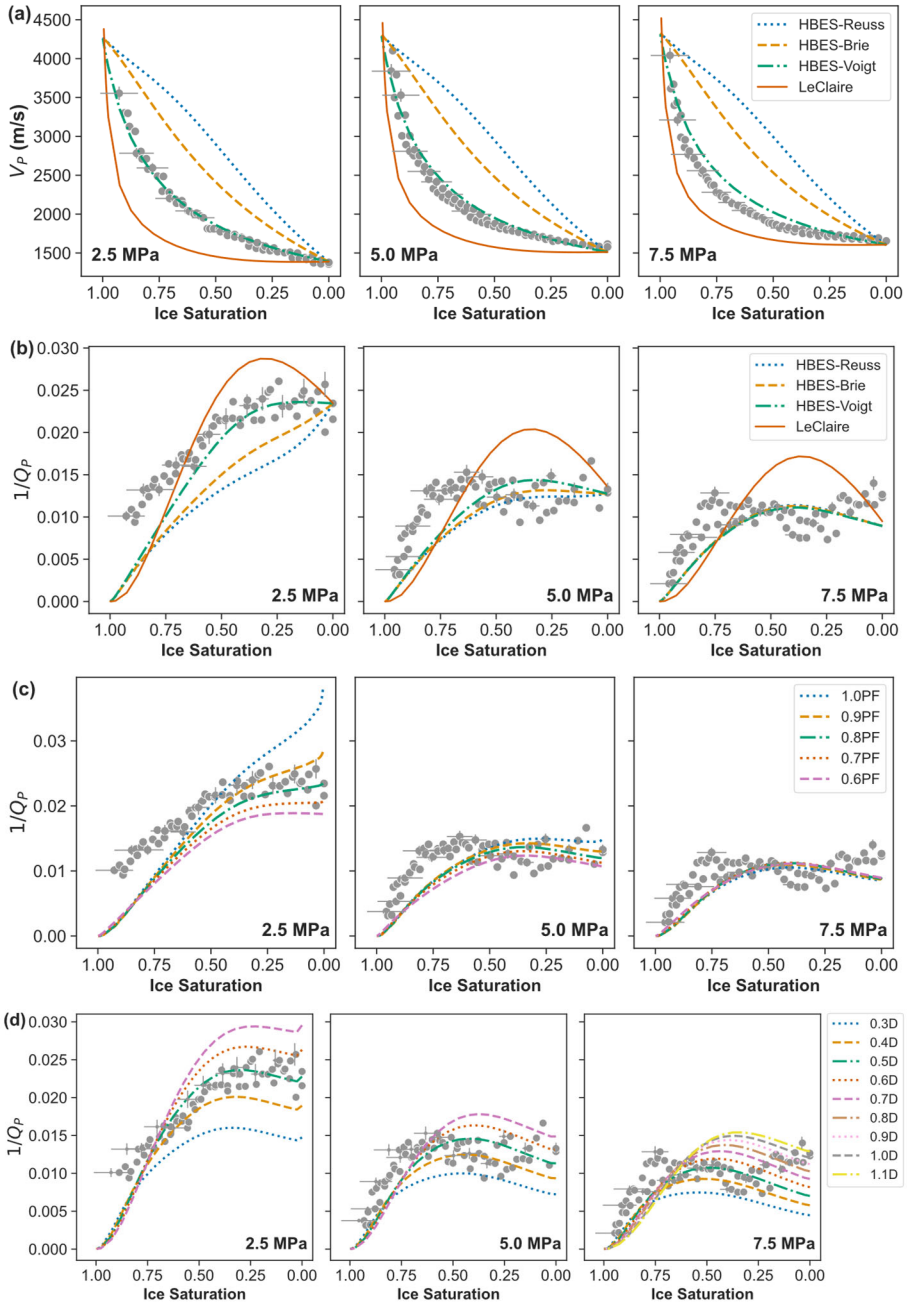

Figure 7 Comparison of experimental data and model results for P-waves at 10 kHz: a) velocity (V_P) and b) attenuation ($1/Q_P$). In the HBES models, the pore-filling saturation PF is 1.0 and the permeability is 0.5 D; c) attenuation at different PF (with the remainder of S_i as cementing ice, i.e., 1 - PF); and d) attenuation at different permeabilities for PF = 1.0. Results in c) and d) are modeled using the HBES model with Voigt approximation. Cross-error bars are plotted every 15 experimental data points.

873x1255mm (330 x 330 DPI)

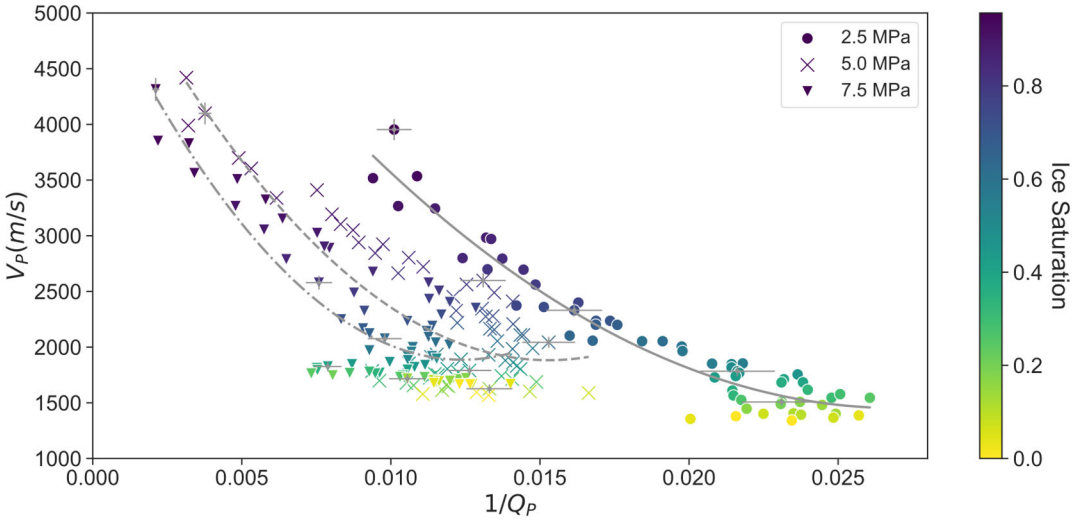

Figure 8 Variations in P-wave velocity (V_P) and attenuation ($1/Q_P$) at 10 kHz plotted against each other, with lines representing second-order polynomial regression models with R^2 of 0.94, 0.72, and 0.72 at 2.5, 5, and 7.5 MPa, respectively. Marker types represent different effective pressures as shown in the legend. Cross-error bars are plotted every 15 data points.

1588x777mm (400 x 400 DPI)

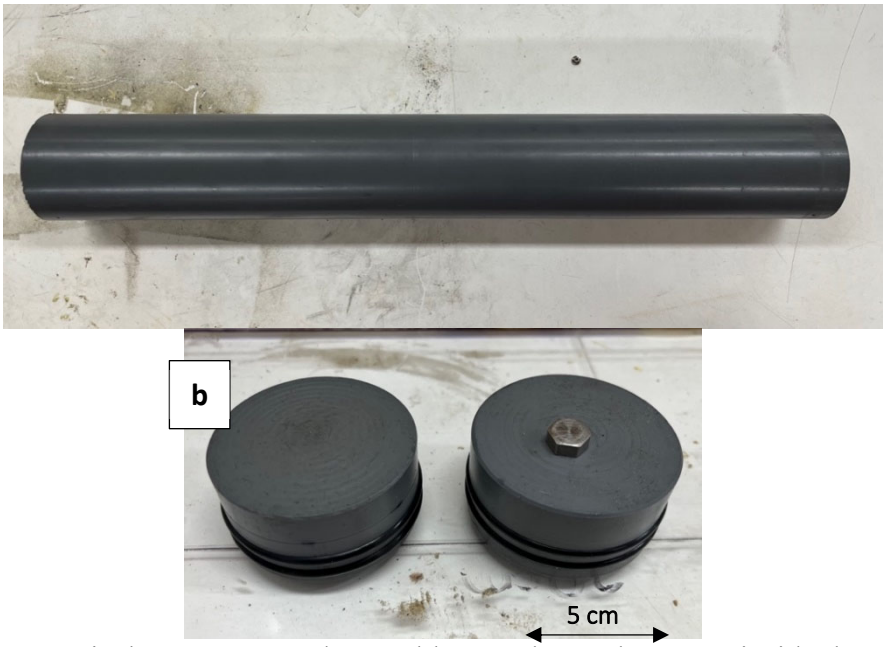

Figure A.1 PVC jacket system used to enable sample emplacement inside the water-filled acoustic pulse tube: a) 50 cm length PVC cylinder jacket, and b) top and bottom PVC endcaps with O-ring seals, including the location of the pore fluid vent port (shown as a hexagonal nut on the top endcap on the right).
355x131mm (220 x 220 DPI)

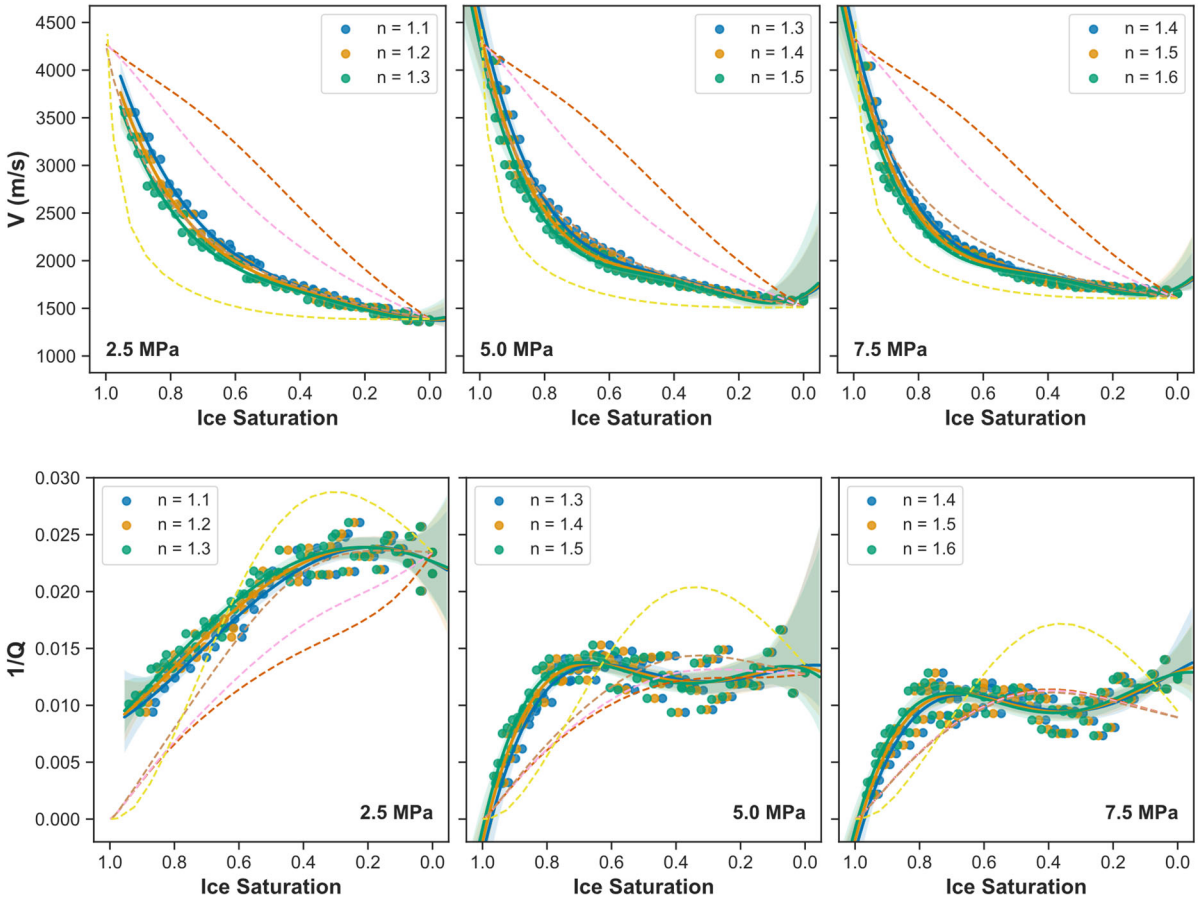

Figure B.1 Empirical parameter (n) fitting of measured data at 10 kHz (indicated by the legend) of velocity (top) and attenuation (bottom) to HBES with Reuss, Brie, and Voigt approximations (red, pink, and brown dashed lines, respectively) and LeClaire (yellow dashed lines) models. Blue, orange, and green lines represent the respective regression models for each dataset, with an averaged R^2 of 0.98 and 0.85 for velocity and attenuation, respectively.

690x622mm (192 x 192 DPI)

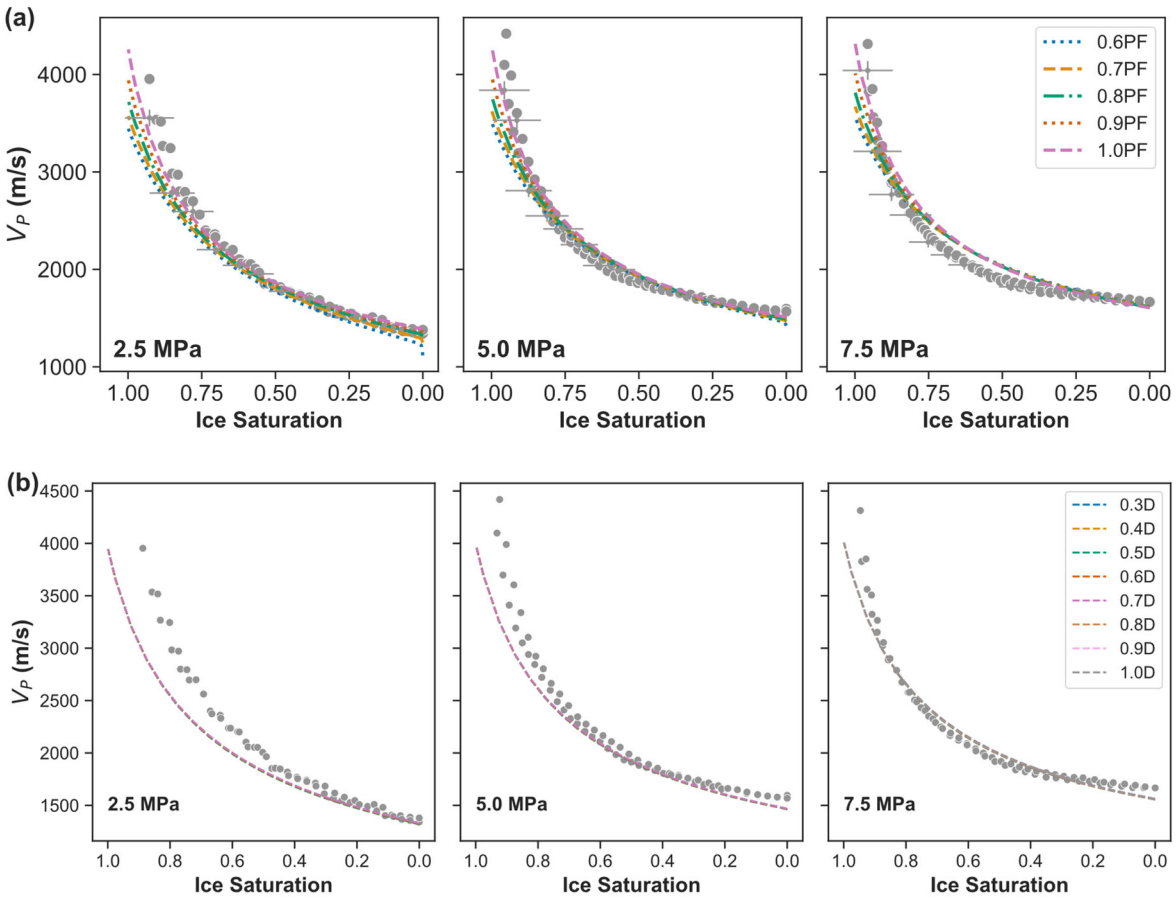

Figure B.2 Comparison of experimental (data points) and modeled velocities (dashed lines): a) at various pore-filling (PF) saturation of ice, and b) at various permeabilities (in Darcies [D] = 1 x 10^{-12} m^2) for PF = 1.0, using the HBES model with Voigt approximations.

690x622mm (192 x 192 DPI)

Table 1 Fixed input parameters that are used in all model runs and case-dependent parameters that are used only in HBES model runs.

Parameter	Value	Units	Reference
Fixed input parameters			
Experimental conditions			
Effective pressure (P_{eff})	2.5, 5.0, 7.5	MPa	
Temperature	19	^{o}C	
Sand sediment properties			
Porosity without ice	0.41		Measured
Critical porosity	0.38		Best et al. (2013)
Sand grain bulk modulus	36×10^9	Pa	Simmons (1965)
Sand grain shear modulus	45×10^9	Pa	Simmons (1965)
Sand grain density	2650	Kg m^{-3}	Simmons (1965)
Sand grain diameter	10^{-4}	m	Best et al. (2013)
Coordination number	9		Murphy (1982)
Tortuosity	3		Berryman (1981)
Ice grain properties			
Ice bulk modulus	5.5×10^9	Pa	Chang et al. (2021)
Ice shear modulus	2.7×10^9	Pa	Chang et al. (2021)
Case-dependent input parameters			
Pore-filling saturation	0.6 – 1.0		
Sand column permeability	0.3 – 1.1	Darcy	

Table B.1 Calculation of objective functions to compare experimental and modelled velocity and attenuation. Best fits are indicated by lowest values (underlined).

Dataset	Objective function at n =				
	1.1	**1.2**	**1.3**	**1.4**	**1.5**
2.5 MPa	0.359	0.349	0.351	0.359	0.375
5 MPa	0.317	0.416	0.314	0.403	0.333
7.5 MPa	0.721	0.655	0.596	0.531	0.467

DATA AND MATERIALS AVAILABILITY

Data associated with this research are available and can be obtained by contacting the corresponding author.